Constraints on axion dark matter with pulsar timing array

Kato, Ryo

(Degree)
博士（理学）

(Date of Degree)
2020-03-25

(Date of Publication)
2021-03-01

(Resource Type)
doctoral thesis

(Report Number)
甲第7700号

(URL)
https://hdl.handle.net/20.500.14094/D1007700

Doctoral Dissertation

Constraints on axion dark matter with pulsar timing array

パルサータイミングアレイによるアクシオンダークマターへの制限

January 2020

Graduate School of Science, Kobe University

Ryo Kato

加藤亮

Abstract

An ultralight scalar field is a candidate for the dark matter. The Pulsar Timing Array offers a unique opportunity to search for the ultralight scalar field with mass around 10^{-23} eV. The dark matter makes up about 30 percent of the cosmic components, and the detection is very important. In particular, the ultralight scalar dark matter can solve the core-cusp problem of galactic halos.

We search for the ultralight scalar dark matter using the North American Nanohertz Observatory for Gravitational Waves 11-year Data Set. We give the 95% confidence upper limit for the energy density of the ultralight scalar dark matter near the Earth. In comparison with the published upper limits on the ultralight scalar dark matter using the Parkes Pulsar Timing Array 12-year data set (Porayko et al. 2018), we find three times stronger upper limit in the mass range from 9.45×10^{-24} to 1.34×10^{-23} eV. In terms of the energy density of the dark matter, we find that the energy density near the Earth is less than $7\,\mathrm{GeV/cm^3}$ in the range from 5.83×10^{-24} to 2.02×10^{-23} eV. The strongest upper limit on the the energy density is given by $2\,\mathrm{GeV/cm^3}$ at a mass 1.09×10^{-23} eV.

Contents

Abstract **1**

1 Introduction **5**
1.1 Why we want to detect FDM? 6
1.2 Why we use pulsar timing array? 6
1.3 Which analysis method is suitable? 7

2 Fuzzy Dark Matter **8**
2.1 Candidate of Fuzzy Dark Matter 8
2.2 Fuzzy Dark Matter in Expanding Universe 9
2.3 Fuzzy Dark Matter Signal 10
2.3.1 Oscillation of Pressure 10
2.3.2 Oscillation of Gravitational Potential 11
2.3.3 Oscillation of Pulse Arrival Time 12

3 Pulsar Timing Array **15**
3.1 Pulsar Timing Array Projects 15
3.2 Timing residual 17
3.2.1 Space and time coordinate 17
3.2.2 Solar system delay 19
3.2.3 Interstellar delay 20
3.2.4 Binary delay 21
3.2.5 Uncertainty of fitting in timing model 22

4 Bayesian analysis in the time domain **24**
4.1 Data 24
4.2 Signal 25
4.3 Model 26
4.4 Likelihood Function and Posterior Probability Distribution 31
4.5 Prior Probability Distribution 35
4.6 Markov chain Monte Carlo simulation 36
4.7 Pre-analysis 37

5 Result **39**
5.1 Upper limits 39
5.2 Fixed noise analysis 41

6 Conclusion **46**

A Bayesian Parameter Estimation and Model Comparison **48**

B Simulated Signal **52**

Conventions

Units:

$$c = G = 1$$

Metric tensor:

$$g_{\mu\nu} = \mathrm{diag}(-,+,+,+)$$

Christoffel symbols：

$$\Gamma^{\mu}{}_{\nu\lambda} = \frac{1}{2} g^{\mu\alpha}(g_{\alpha\nu,\lambda} + g_{\alpha\lambda,\nu} - g_{\nu\lambda,\alpha})$$

Riemann curvature tensor:

$$R^{\mu}{}_{\nu\rho\sigma} = \Gamma^{\mu}{}_{\nu\sigma,\rho} - \Gamma^{\mu}{}_{\nu\rho,\sigma} + \Gamma^{\mu}{}_{\lambda\rho}\Gamma^{\lambda}{}_{\nu\sigma} - \Gamma^{\mu}{}_{\lambda\sigma}\Gamma^{\lambda}{}_{\nu\rho}$$

Ricci tensor:

$$R_{\mu\nu} = R^{\alpha}{}_{\mu\alpha\nu}$$

Curvature scalar:

$$R = g^{\mu\nu} R_{\mu\nu}$$

Einstein tensor:

$$G_{\mu\nu} = R_{\mu\nu} - \frac{1}{2} g_{\mu\nu} R$$

Fourier transform:

$$\begin{aligned} g(t) &= \int_{-\infty}^{\infty} df \; \tilde{g}(f) \mathrm{e}^{-i2\pi ft} \\ \tilde{g}(f) &= \int_{-\infty}^{\infty} dt \; g(t) \mathrm{e}^{i2\pi ft} \end{aligned}$$

Chapter 1

Introduction

The dark matter problem is clearly one of the most important issues in modern cosmology. Recently, motivated by string theory, an ultralight scalar dark matter has been intensively studied [1, 2]. In particular, an ultralight scalar field with mass 10^{-23} eV can behave like the cold dark matter (CDM) on cosmological scales and resolve a core-cusp problem [3, 4]. In this thesis, we call it simply the fuzzy dark matter (FDM). The FDM can be treated as a classical scalar field because the occupation number of the FDM accounting for the energy density of the dark matter is very large. The main difference between FDM and CDM is that the pressure of the FDM is coherently oscillating, while that of CDM almost vanishes. Khmelnitsky and Rubakov have pointed out that the effect of oscillating pressure might be detected with the pulsar timing arrays (PTAs) [5]. Indeed, the oscillation of the pressure induces the oscillation of the gravitational potential, and as a result, it induces the oscillation of the arrival time of the pulse passing through the gravitational potential.

Nowadays, the PTAs are most sensitive to the gravitational effects with a few nanohertz frequency. There are three major pulsar timing projects: the European Pulsar Timing Array (EPTA) [6], the North American Nanohertz Observatory for Gravitational Waves (NANOGrav) [7], and the Parkes Pulsar Timing Array (PPTA) [8]. The collaboration of the three projects is called the International Pulsar Timing Array (IPTA) [9]. Furthermore, observations of the pulsars have started by Five-hundred-meter Aperture Spherical Telescope (FAST) in China and MeerKAT in South Africa. From 2020 year, the Square Kilometre Array (SKA) will begin observations which is the next generation telescope. There are many projects observing the pulsars, therefore, the PTA is currently receiving much interest.

Porayko and Postnov [10] gave upper limits for the FDM with the Bayesian analysis using the NANOGrav 5-year Data Set. Moreover, Porayko et al. [11] gave upper limits for the FDM with the Bayesian and the Frequentist analyses using the PPTA 12-year Data Set. Following the previous articles, we search for the FDM by the Bayesian analysis in the time domain using the NANOGrav 11-year Data Set. We quantitatively investigate whether the ultralight scalar dark matter is detectable or not using the Bayesian model selection approach. We clarify the prior dependence of constraints

on the amplitude of the FDM signal and obtain three times stronger constraints on the amplitude of the FDM signal in the frequency range from $10^{-8.34}$ to $10^{-8.19}$ Hz. We also discuss how the results of Bayesian analysis depend on the solar system ephemeris noise in the model describing the observation data.

1.1 Why we want to detect FDM?

In the first place, it is known that the percentage of the dark matter in the universe is 26% based on the CMB observations by the Planck satellite. For this reason, the detection of the dark matter is one of the important issues in physics. Currently, various unknown particles are considered as dark matter candidates. Some of the dark matter candidates include the FDM, the neutralino of supersymmetric particles, the sterile neutrino that interact only with gravity, and the black hole in the early universe.

The reason for searching for the FDM is that the FDM can solve the core-cusp problem if the mass is about 10^{-23} eV/c^2 [3, 4]. The core-cusp problem is a problem in which the energy density of the dark matter halo does not agree between the theory and the observation. Theoretically, the energy density increases as it approaches the center of the galaxy, but in observation, it is a constant value at the center of the galaxy.

The FDM can solve the core-cusp problem because its mass is so small that it becomes wavelike at the galactic scale. Actually, the de Broglie wavelength λ is on the order of the galaxy scale:

$$\lambda = \frac{2\pi\hbar}{mv} \sim 4 \text{ kpc} \left(\frac{10^{-23}\text{eV/c}^2}{m}\right)\left(\frac{10^{-3}c}{v}\right), \tag{1.1.1}$$

where v is the typical velocity of the matter in the galaxy. Therefore, the FDM can be made to have a core structure at the center of the galaxy by spreading to the de Broglie wavelength.

1.2 Why we use pulsar timing array?

In the first place, the pulsar timing array is used to detect the gravitational waves and is the highest precision detector. Since the article [5] revealed that the pulsar timing array can detect the FDM, it would be natural to attempt detection with the pulsar timing array. However, recent observations have limited the low mass FDM that can be detected with a pulsar timing array. For example, if the FDM mass is less than 10^{-22} eV/c^2, from the observation of the Lyman-alpha forest, the proportion of FDM in dark matter is less than 20% [12], see figure 1.1. Therefore, there is a relatively strong constraint on the FDM that can be detected by the pulsar timing array. Currently, the pulsar timing array is not sensitive enough to detect FDM. However, if sensitivity is improved by the SKA, it is expected that a constraint comparable to that of Lyman-alpha forest will be obtained [5]. In addition, the constraints of the Lyman-alpha forest and the pulsar timing array are obtained on the cosmological scale and the galactic scale, respectively. It would be important to confirm that these two constraints of different scales are consistent.

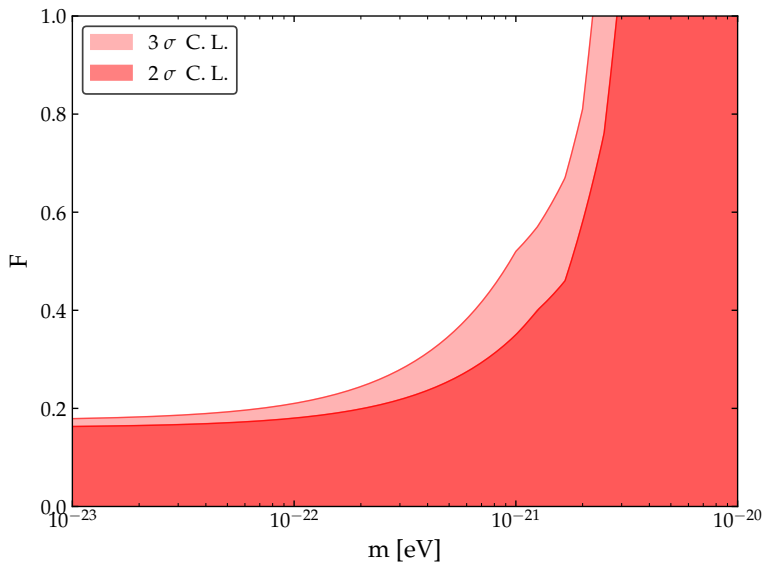

Figure 1.1: Lyman-alpha forest constraint which is obtained by the article [12]. The vertical axis is the proportion of the FDM in the dark matter, and the horizontal axis is the FDM mass.

1.3 Which analysis method is suitable?

In general, there are two ways of interpreting probabilities: frequentist and Bayesian. In the pulsar timing array, the number of parameters for parameter estimation is very large, and the likelihood function is multimodal. Therefore, it is more reasonable to estimate the likelihood function rather than to derive an analytical (or numerical) solution for the parameter that maximizes the likelihood function. In the Bayesian, a method for estimating the posterior distribution obtained by multiplying the likelihood function by the prior distribution is known, which is called Markov chain Monte Carlo method (MCMC). Therefore, we will use the Bayesian statistics instead of frequentist statistics.

In data analysis, it is important whether the data is handled in the time domain or the Fourier domain. The data used in the pulsar timing array is obtained by irregular observation intervals. The Fourier transform assumes uniform sampling, so the nature of the observation data in the Fourier domain of PTA is not well understood. In a pulsar timing array, it would be natural to handle data in the time domain. Therefore, we will use the data in the time domain.

Chapter 2

Fuzzy Dark Matter

The cosmological model containing cold dark matter and dark energy can explain the CMB observations very well. However, in astrophysical scales, the density profile of the galaxy halo predicted by the cold dark matter model does not match the actual galaxy profile. This disagreement is called the core-cusp problem. To solve the core-cusp problem, an ultra-light scalar field was introduced as a candidate for the dark matter. The ultralight scalar field is called the fuzzy dark matter.

2.1 Candidate of Fuzzy Dark Matter

In this section we review the axion which is a candidate for the FDM, see the articles [1, 13, 14] for further detail. The axion is a pseudo Nambu-Goldstone boson, which is introduced when global symmetry breaks spontaneously. There are two parameters that characterize the axion. The first is the parameter F, which is related to the scale of the spontaneous symmetry breaking. The second is the parameter μ, which is related to the scale at which the instanton effect occures. Due to the instanton effect, the shift symmetry of the axion is broken explicitly and the axion can have a mass. It is known that the Lagrangian for the axion can be written as follows:

$$\mathcal{L} = \frac{1}{2}\partial_\mu\phi\partial^\mu\phi - \mu^4\left[1 - \cos\left(\frac{\phi}{F}\right)\right], \tag{2.1.1}$$

where ϕ denotes the axion. As can be seen from this equation, the symmetry of the Lagrangian is discrete $\phi \to \phi + 2\pi F$, due to the second term. Expanding the second term to the quadratic order in the axion, we can define the axion mass as

$$m \equiv \frac{\mu^2}{F}. \tag{2.1.2}$$

Considering the behavior of the axion with mass 10^{-22}eV in the expanding universe, the value of the F is known to be as follows [14]:

$$F \sim 0.5 \times 10^{17}\text{GeV}. \tag{2.1.3}$$

The value in the above equation is between the grand unified scale $M_G \sim 10^{16}$GeV and the reduced Planck mass $M_{\rm Pl} \sim 10^{18}$GeV, and it is known that this parameter space is preferred in string theory. Then the energy density of the axion is close to the percentage the dark matter in the universe:

$$\Omega_{\rm axion} \sim 0.1 \left(\frac{F}{10^{17}{\rm GeV}}\right)^2 \left(\frac{m}{10^{-22}.{\rm eV}}\right)^{1/2}. \tag{2.1.4}$$

2.2 Fuzzy Dark Matter in Expanding Universe

In this section, we describe that FDM behaves as dark energy in the early expanding universe and dark matter in later expanding universe. After inflation, the universe expands depending on what components of the universe are dominant. There are three eras in the expanding universe; radiation dominant, matter dominant, and dark energy dominant. First, in the early expanding universe, the radiation is dominant, and the energy density of the radiation is inversely proportional to the fourth power of the scale factor. The scale factor is a time-dependent variable that describes the expansion of the universe. Next, in the later expanding universe, the matter is dominant, and the energy density of the matter is inversely proportional to the third power of the scale factor. Finally, in the most recent expanding universe, the dark energy is dominant, and the energy density of the dark energy is constant independent of the scale factor.

The FDM mass is very small, so that the large occupation number would be required. This means that FDM can be regarded as a classical field. The action for the FDM with the flat FLRW metric $ds^2 = -c^2dt^2 + a^2(t)\left[dx^2 + dy^2 + dz^2\right]$ is

$$S_\phi = \int d^4x\ a^3(t) \left[\frac{1}{2}\partial^\mu\phi\partial_\mu\phi - \frac{1}{2}m^2\phi^2\right], \tag{2.2.1}$$

where $a(t)$ is the scale factor. Then the equation of motion for the FDM is

$$\ddot{\phi} + 3H\dot{\phi} + m^2\phi = 0, \tag{2.2.2}$$

where $H \equiv \dot{a}/a$ is the Hubble parameter. Therefore, the behavior of the FDM changes depending on the magnitude relationship between the Hubble parameter and the FDM mass.

In the early expanding universe, the relationship $H \gg m$ holds, because the Hubble parameter decreases as the universe expands. Assuming the relationship $H \gg m$, Eq. (2.2.2) gives the following solution:

$$\phi = C_1 + C_2 \int a^{-3}\, dt, \tag{2.2.3}$$

where C_1 and C_2 are the constants. The second term in the above equation denotes that FDM approaches a certain value as the scale factor increases. Therefore, in the early

expanding universe, FDM can be considered almost constant independent of time. As described in the next section, the energy density of FDM would be

$$\rho = \frac{1}{2}\dot{\phi}^2 + \frac{1}{2}m^2\phi^2. \tag{2.2.4}$$

Due to $\phi \simeq$ const, the above equation means that the FDM is almost independent of the scale factor. Therefore, in the early expanding universe, the FDM can be considered as dark energy which is constant independent of the scale factor.

In the later expanding universe, the relationship $H \ll m$ holds. Since it is the later expanding universe, assuming the mater dominant $a \propto t^{2/3}$, Eq. (2.2.2) gives the following solution:

$$\phi = C_3\frac{\sin(mt)}{t} + C_4\frac{\cos(mt)}{t}, \tag{2.2.5}$$

where C_3 and C_4 are the constants. Substituting this equation into Eq. (2.2.4), then taking time average with about $1/m$ time, the energy density is

$$\langle\rho\rangle \propto \frac{1}{t^2} \tag{2.2.6}$$

Due to the mater dominant $a \propto t^{2/3}$, the above equation means that the FDM is inversely proportional to the third power of the scale factor. Therefore, in the later expanding universe, the FDM can be considered as the matter (almost dark matter) which is inversely proportional to the third power of the scale factor.

2.3 Fuzzy Dark Matter Signal

The pulsar timing array can detect the time oscillation of the arrival time of the pulse. In this section, we derive the time oscillation of the arrival time of the pulse which induced by the FDM. The derivation is based on the article [5]. This article show that the FDM can be regarded as a perfect fluid with oscillating pressure. Then the oscillation of the pressure induces the oscillation of the gravitational potential. Finally, it induces the oscillation of the arrival time of the pulse passing through the gravitational potential. We will refer to this oscillation as the FDM signal. The purpose of this thesis is to detect the FDM signal using the pulse timing array.

As mentioned in the following subsection 2.3.3, the FDM signal is a simple sine wave, and so some noise in the data may have a similar waveform. Therefore, it is necessary to consider whether the FDM signal obtained by data analysis is the actual FDM signal or some noise.

2.3.1 Oscillation of Pressure

In this subsection, we derive the energy momentum tensor for the FDM, and show that the energy momentum tensor is the perfect fluid with oscillating pressure. First,

assuming that the FDM velocity is the nonrelativistic in the galaxy, the dispersion relation is

$$E_k^2 = m^2 + k^2 = m^2 + (mv)^2 \simeq m^2, \tag{2.3.1}$$

where $v \approx 10^{-3}$ is the typical velocity of matters in the galaxy. Then the plane wave solution of the Klein-Gordon equation is monochromatic as follows:

$$\phi(t, \mathbf{x}) = \phi_0(\mathbf{x}) \cos(mt + \alpha(\mathbf{x})). \tag{2.3.2}$$

The energy momentum tensor is

$$T_{\mu\nu} = \partial_\mu \phi \partial_\nu \phi - \frac{1}{2} \left((\partial\phi)^2 + m^2 \phi \right) \eta_{\mu\nu}. \tag{2.3.3}$$

Substituting Eq. (2.3.2) into the above equation, under the relation

$$\partial_i \phi \ll \partial_0 \phi \quad \because k \ll m, \tag{2.3.4}$$

we can obtain

$$\begin{aligned} T_{00} &= \frac{1}{2}\dot{\phi}^2 + \frac{1}{2}m^2\phi^2 = \frac{1}{2}m^2\phi_0^2 = \rho, \\ T_{ij} &= \left(\frac{1}{2}\dot{\phi}^2 - \frac{1}{2}m^2\phi^2 \right) \delta_{ij} = -\frac{1}{2}m^2\phi_0^2 \cos(2mt + 2\alpha)\delta_{ij} = -\rho \cos(2mt + 2\alpha)\delta_{ij}, \end{aligned} \tag{2.3.5}$$

where we defined the energy density of the FDM $\rho \equiv 1/2m^2\phi_0^2$. Therefore, the nonrelativistic classical scalar field behaves as a perfect fluid with an oscillating pressure.

2.3.2 Oscillation of Gravitational Potential

In this subsection we show that the oscillating pressure induces the oscillation of the gravitational potential. The linearized Einstein equation is

$$G_{\mu\nu} = 8\pi G T_{\mu\nu}. \tag{2.3.6}$$

Using the Newtonian gauge

$$ds^2 = -(1 - 2\Psi)dt^2 + (1 + 2\Psi)\delta_{ij}dx^i dx^j, \tag{2.3.7}$$

the Einstein tensor are calculated as follows:

$$\begin{aligned} G_{00} &= -2\Psi^{,i}{}_{,i}, \\ G_{0i} &= G_{i0} = -2\dot{\Psi}_{,i}, \\ G_{ij} &= -2\ddot{\Psi}\delta_{ij}. \end{aligned} \tag{2.3.8}$$

Let us divide the gravitational potential into time-independent part and time-dependent perturbation part

$$\Psi = \Psi_0(\mathbf{x}) + \delta\Psi(t, \mathbf{x}), \quad |\Psi_0(\mathbf{x})| \gg |\delta\Psi(t, \mathbf{x})|. \tag{2.3.9}$$

Then, Eq. (2.3.8) can be rewritten as follows:

$$\begin{aligned} G_{00} &= -2\Psi_0(\mathbf{x})^{,i}{}_{,i}, \\ G_{0i} &= G_{i0} = -2\delta\dot{\Psi}(t, \mathbf{x})_{,i}, \\ G_{ij} &= -2\ddot{\delta}\Psi(t, \mathbf{x})\delta_{ij}. \end{aligned} \tag{2.3.10}$$

Using Eq. (2.3.5) and Eq. (2.3.10) , the 00 component and the ij component of the Einstein equation Eq. (2.3.6) are

$$\begin{aligned} -2\Psi_0(\mathbf{x})^{,i}{}_{,i} &= 8\pi G\rho, \\ -2\ddot{\delta}\Psi(t, \mathbf{x})\delta_{ij} &= -8\pi G\rho\cos(2mt + 2\alpha)\delta_{ij}. \end{aligned} \tag{2.3.11}$$

The first equation denotes the Poisson equation for the time-independent part. The time-independent gravitational potential does not cause the oscillation of the light arrival time, so that it cannot be detected. On the other hand, the second equation shows that the time-dependent part oscillates. Solving the second equation, we can obtain the oscillation of the gravitational potential:

$$\delta\Psi = \frac{\pi G\rho}{m^2}\cos(2mt + 2\alpha). \tag{2.3.12}$$

This oscillation would cause the oscillation of the light arrival time, and can be detected by the pulsar timing array. From the above, it is understood that the oscillation of the pressure causes the oscillation of the gravitational potential.

2.3.3 Oscillation of Pulse Arrival Time

In this subsection we show that the oscillation of the gravitational potential induces the oscillation of the pulse arrival time. The derivation is based on the articles [15, 16]. We need to solve the geodesic equation to see if the oscillating gravitational potential defined by Eq. (2.3.12) actually causes the oscillation of the light arrival time. The zero component of the geodesic equation is

$$\frac{d^2x^0}{d\lambda^2} + \Gamma^0_{\nu\rho}\frac{dx^\nu}{d\lambda}\frac{dx^\rho}{d\lambda} = 0, \tag{2.3.13}$$

where λ is the affine parameter. By solving the zero component of the geodesic equation, we can obtain the change in the light frequency, that is, the change in the arrival time of the light. First, the world line is written in the zero-order and first-order as follows

$$x^\alpha = x^\alpha_0(\lambda) + x^\alpha_1(\lambda). \tag{2.3.14}$$

Similarly, the four-momentum $k^\alpha \equiv dx^\alpha/d\lambda$ is

$$k^\alpha = k_0^\alpha(\lambda) + k_1^\alpha(\lambda), \tag{2.3.15}$$

where we define the zero-order world line and four-momentum as

$$x_0^\alpha(\lambda) = \omega_0(\lambda, -\lambda\hat{p}) + (t_0, \mathbf{0}), \quad k_0^\alpha = \omega_0(1, -\hat{p}) \tag{2.3.16}$$

ω_0 denotes zero-order frequency and $\hat{p} \equiv \mathbf{x}_p/|\mathbf{x}_p|$ denotes the unit vector for pulsar direction. We also define the zero-order affine parameters of the earth and the pulsar:

$$\lambda_{0e} = 0, \quad \lambda_{0p} = -\frac{|\mathbf{x}_p|}{\omega_0}. \tag{2.3.17}$$

When affine parameters are defined in this way, the light observed on the earth at the origin of the spatial coordinates at time t_0 is emitted at time $t_0 - |\mathbf{x}_p|$ at the position $\mathbf{x}_p$ of the pulsar in zero-order. Then the zero component of the first order of the geodesic equation is

$$\begin{aligned}
\frac{d^2x_1^0}{d\lambda^2} &= -\Gamma^0_{00}\frac{dx^0}{d\lambda}\frac{dx^0}{d\lambda} - \Gamma^0_{0i}\frac{dx^0}{d\lambda}\frac{dx^i}{d\lambda} - \Gamma^0_{i0}\frac{dx^i}{d\lambda}\frac{dx^0}{d\lambda} - \Gamma^0_{ij}\frac{dx^i}{d\lambda}\frac{dx^j}{d\lambda} \\
&= \dot{\Psi}\frac{dx_0^0}{d\lambda}\frac{dx_0^0}{d\lambda} + 2\Psi_{,i}\frac{dx_0^0}{d\lambda}\frac{dx_0^i}{d\lambda} - \dot{\Psi}\delta_{ij}\frac{dx_0^i}{d\lambda}\frac{dx_0^j}{d\lambda} \\
&= 2\omega_0^2\Psi_{,i}p^i,
\end{aligned} \tag{2.3.18}$$

where p^i expresses the vector $\hat{p}$ in component form. The zero component of the first-order four-momentum can be obtained by integrating the above equation with an affine parameter, where the integration interval can be defined with a zero-order affine parameter because the integrand is already in the first order, namely

$$k_1^0(\lambda) = 2\omega_0^2\int_0^\lambda d\lambda'\ \Psi_{,i}p^i + I_0, \tag{2.3.19}$$

where I_0 is the integration constant. Next, we calculate the integration constant. The frequency of light which is emitted at an object with the four velocity u^μ is

$$\omega = -g_{\mu\nu}k^\mu u^\nu. \tag{2.3.20}$$

Therefore, when the pulser emits the light with frequency ω_0 at λ_{0p}, the frequency of light is

$$\begin{aligned}
\omega_0 &= -g_{\mu\nu}(\lambda_{0p})k^\mu(\lambda_{0p})u^\nu(\lambda_{0p}), \\
&= (1 - 2\Psi(\lambda_{0p}))k^0(\lambda_{0p})(1 + \Psi(\lambda_{0p})), \\
&= (1 - 2\Psi(\lambda_{0p}))(k^0(\lambda_{0p}^0) + k^0(\lambda_{0p}^1))(1 + \Psi(\lambda_{0p})), \\
&= (1 - 2\Psi(\lambda_{0p}))\left(\omega_0 + 2\omega_0^2\int_0^{\lambda_{0p}} d\lambda'\ \Psi_{,i}p^i + I_0\right)(1 + \Psi(\lambda_{0p})), \\
&= \omega_0(1 - \Psi(\lambda_{0p})) + 2\omega_0^2\int_0^{\lambda_{0p}} d\lambda'\ \Psi_{,i}p^i + I_0(1 - \Psi(\lambda_{0p})).
\end{aligned} \tag{2.3.21}$$

From the above equation, the integration constant is as follows:

$$I_0 = \omega_0 \Psi(\lambda_{0p}) - 2\omega_0^2 \int_{\lambda_{0e}}^{\lambda_{0p}} d\lambda' \ \Psi_{,i} p^i. \tag{2.3.22}$$

Therefore, the frequency of light ω_{obs} observed on the earth at λ_{0e} is

$$\begin{aligned}
\omega_{obs} &= -g_{\mu\nu}(\lambda_{0e}) k^\mu(\lambda_{0e}) u^\nu(\lambda_{0e}), \\
&= (1 - 2\Psi(\lambda_{0e})) k^\mu(\lambda_{0e})(1 + \Psi(\lambda_{0e})), \\
&= (1 - 2\Psi(\lambda_{0e}))(\omega_0 + I_0)(1 + \Psi(\lambda_{0e})), \\
&= \omega_0(1 - \Psi(\lambda_{0e})) + \omega_0 \Psi(\lambda_{0p}) - 2\omega_0^2 \int_{\lambda_{0e}}^{\lambda_{0p}} d\lambda' \ \Psi_{,i} p^i, \\
&= \omega_0 + \omega_0(\Psi(\lambda_{0p}) - \Psi(\lambda_{0e})) - 2\omega_0^2 \int_{\lambda_{0e}}^{\lambda_{0p}} d\lambda' \ \Psi_{,i} p^i. \qquad (2.3.23)
\end{aligned}$$

The third term in the above equation is negligible because we can only detect the oscillation part of the gravitational potential $\delta\Psi$. The oscillation time $1/2m$ of the gravitational potential $\delta\Psi$ is much smaller than propagation time between the pulsar and the earth.

Then, the red shift of light z is

$$\begin{aligned}
z &\equiv \frac{\omega_0 - \omega_{obs}}{\omega_0} \\
&= \Psi(\lambda_{0e}) - \Psi(\lambda_{0p}). \qquad (2.3.24)
\end{aligned}$$

Finally, the deviation of the light arrival time Δt can be obtained by integrating the redshift with observation time, so

$$\Delta t = \int_0^t dt \ z, \tag{2.3.25}$$

$$= \int_0^t dt \ \Psi(\lambda_{0e}) - \Psi(\lambda_{0p}). \tag{2.3.26}$$

Since the pulsar cannot be detected if the arrival time of light is not oscillating, rewriting only with the gravitational potential oscillating in time Eq. (2.3.12), the FDM signal $s(t)$ is

$$\Delta t = \frac{1}{2\pi f}[\Psi_0(\mathbf{x_e}) \sin(2\pi f t + 2\alpha(\mathbf{x_e})) - \Psi_0(\mathbf{x_p}) \sin(2\pi f(t - D) + 2\alpha(\mathbf{x_p}))] \equiv s(t), \tag{2.3.27}$$

where $f = m/\pi$ is a frequency, $\Psi_0 \equiv \pi G\rho/m^2$, D is the distance between the pulsar and the earth, each $\mathbf{x_e}$ and $\mathbf{x_p}$ are the position of the Earth and the pulsar. The FDM signal can be observed as the periodic signal with the frequency determined by the mass of the FDM. From the above, the oscillation of the gravitational potential induces the oscillation of the pulse arrival time

Chapter 3

Pulsar Timing Array

First of all, a pulsar is a fast rotating neutron star. The figure 3.1 denotes the pulsar. The beam from the pulsar can be received as a pulse on the earth because the rotation axis and the beam axis of the pulsar are different. As a feature of pulsars, some pulsars are known to have an accuracy of pulse period comparable to that of atomic clocks, so they can be regarded as natural clocks in the universe [17]. In addition, thousands of pulsars will be observed in the Milky Way Galaxy [18]. Due to these features, long-term observation of a large number of pulsars is expected to detect pulse period deviations caused by gravitational effects. Numerous pulsars in the Milky Way Galaxy constitute the galaxy-scale gravitational effect detectors, which is called the pulsar timing arrays.

The concept of the pulsar timing array originated from the American community in 1989 [19, 20]. This community proposed an attempt to detect a stochastic gravitational wave background by observing many pulsars over the long term. To date, several pulsar timing array projects have aimed to detect the stochastic gravitational wave background. Here, the fuzzy dark matter is an exotic target, not the main target of the pulsar timing array.

3.1 Pulsar Timing Array Projects

There are three main pulsar timing array projects and their collaboration:

- The Parkes Pulsar Timing Array (PPTA) [8]

  The PPTA was established in 2004. The PPTA uses the Parkes radio telescope in New South Wales, Australia. The feature is that unlike other projects, the pulsar in the southern hemisphere can be observed. In the southern hemisphere sky, there is a pulsar with the highest pulse period accuracy of PSR J0437-4715.

- The European Pulsar Timing Array (EPTA) [6]

  The EPTA was established in 2006. The EPTA is a European collaboration. The EPTA uses five telescopes, Effelsberg, Lovell, Nançay, Sardinia, and Westerbork

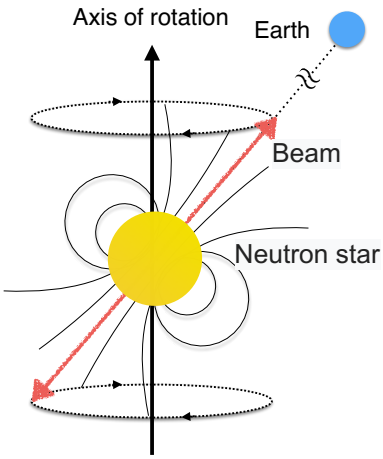

Figure 3.1: Pulsar

in Europe. Since it has five telescopes, it can observe pulsars more frequently than other projects. Effectively, observation data can be made once a week.

- The North American Nanohertz Observatory for Gravitational waves (NANOGrav) [7]

  The NANOGrav was established in 2007. The NANOGrav uses two telescopes, Green Bank and Arecibo, in the United States. The Arecibo telescope is the second largest in the world and very sensitive to pulses. The Green Bank telescope is the world's largest movable telescope. The area of the sky that can be covered is small compared to other projects because the Arecibo terescope cannot be moved.

- The International Pulsar Timing Array (IPTA) [9]

  The IPTA is is a consortium of consortia, comprised of the PPTA, the EPTA and the NANOGrav mentioned above. The IPTA aims at detection of background gravitational waves by combining pulsar observation data from each project. In 2016, the noise contained in the pulsar observation data was estimated, and an upper limit was given to the amplitude of the stochastic gravitational wave background [21].

Other than the above projects, observations of pulsars have started by Five-hundred-meter Aperture Spherical Telescope (FAST) in China and MeerKAT in South Africa.

The Square Kilometre Array project [22] is an international attempt to construct a next-generation radio telescope, and observations will begin in 2020. The five major key sciences of Square Kilometre Array are the evolution of galaxies, the verification of gravity theory, the evolution of the cosmic magnetic field, the dark era of the universe, and the life in the universe. The second key science, verification of gravity theory, corresponds to the pulsar timing array.

3.2 Timing residual

In the pulsar timing, the data analysis is performed on the residual, not the time-of-arrival (TOA) of the pulse from the pulsar. The residual is defined as the TOA minus the timing model [23]. The residual calculation is done with TEMPO2 [24].[1)] The timing model predicts the time from when a pulse is emitted until when it is detected. The timing model in time is represented by the following three effects:

$$t_{\rm psr} = t_{\rm obs} - \Delta_{\odot} - \Delta_{\rm IS} - \Delta_{\rm B}, \tag{3.2.1}$$

where $t_{\rm psr}$ is the pulse emission time, $t_{\rm obs}$ is the TOA of the pulse at the observatory, $\Delta_{\odot}$ includes the effects which are induced in the solar system, $\Delta_{\rm IS}$ includes the effects which are induced in the interstellar, and $\Delta_{\rm B}$ includes the effects which are induced in the binary pulsar if pulsar is binary pulsar. When $\Delta_{\odot}$, $\Delta_{\rm IS}$, and $\Delta_{\rm B}$ are positive, these effects induce the delay of TOA. The effect that is not included in Eq. (3.2.1) is an offset between different receivers and backend systems (known as a JUMP).

In addition, the delay of the arrival time of the pulse also occurs due to a decrease in the rotation speed of the pulser. Due to the evolution of the pulse phase, the timing model in phase is

$$\phi(t) = \phi_0 + \nu(t_{\rm psr} - t_0) + \dot{\nu}(t_{\rm psr} - t_0)^2 + \cdots , \tag{3.2.2}$$

where ϕ_0 is the initial phase, and ν and $\dot{\nu}$ is the expansion coefficient of the frequency of the pulsar. ν and $\dot{\nu}$ are called spin and spin-down parameter, respectively.

In fact, there is uncertainty in principle when fitting timing model parameters. Considering this effect, we perform data analysis for the residual. Therefore, It would be important to mention what kind of timing model was used. In this section we will briefly review the timing mode used in the NANOgrav 11-year Data Set.

3.2.1 Space and time coordinate

The pulsar timing array attempts to detect very small changes that occur during the decade of observation. Therefore, special care must be taken when selecting time and space coordinate systems.

The important time scales in astronomy are listed below[2)]:

- GPS time: determined from atomic clocks of multiple Global Positioning System satellites.
- UTC (Coordinated Universal Time): basis of civil timekeeping.
- UT1 (Universal Time): time coordinates of the coordinate system that rotates with the rotation of the earth.

[1)] https://bitbucket.org/psrsoft/tempo2.git
[2)] http://www.iausofa.org/2015_0209_C/sofa/sofa_ts_c.pdf

- TAI (International Atomic Time): determined from internationally controlled atomic clocks.
- TCG (Geocentric Coordinate Time):time coordinates of GCRS (Geocentric Celestial Reference System) which is used for objects in the vicinity of the Earth.
- TT (Terrestrial Time): theoretical time scale on rotating geoid (also called mean sea level). linear transformation of TCG.
- TCB (Barycentric Coordinate Time): time coordinates of BCRS (Barycentric Celestial Reference System) which is used for the distant celestial objects and the solar system object.
- TDB (Barycentric Dynamical Time): time coordinates that are close to TT when taking the average. linear transformation of TCB.

To create the residual, the TOA obtained at the observatory on the Earth's surface is first converted into the TOA of the coordinate system of the solar system barycenter (SSB). Since the pulsar is outside the solar system, it would be natural to use the coordinate system of the SSB. Either TCB or TDB is used for the time of the coordinate system of the SSB. TEMPO2 can use both TCB and TDB, and TDB is selected in the NANOgrav. TCB is well defined as BCRS time coordinate, while TDB has been used as a convention and must be interpreted with care. For the interpretation of coordinate systems and physical quantities in TDB, see the article [25].

The relationship between the observatory clock and the corresponding TDB can be obtained by connecting various time scales. The time of the hydrogen-maser clock in the observatory and GPS time are compared daily. For transformation from GPS time to UTC, the circular T of the Bureau international des poids et mesures (BIPM) is used.[3)] For transformation from UTC to TAI, the Bulletin C of the International Earth Rotation and Reference Systems Service (IERS) is used.[4)] For transformation from TAI to TT, the TT(BIPM) of the BIPM is used.[5)] TT(BIPM) is updated every year. The data obtained in 2015 is used in the NANOgrav 11-year Data Set. The transformation from TT to TDB is performed in TEMPO2 internally. The method of the transformation from TT to TDB is based on the article [26]. This transformation uses the relationship between TT and TCG, TCG and TCB, and TCB and TDB.

The spatial coordinates of the BCRS is provided by the solar system ephemeris. The solar system ephemeris is a record of the position and the motion of the barycenter of the solar system objects. There are various the solar system ephemeris. The Jet Propulsion Laboratory (JPL) DE436 [27] is used in the NANOgrav 11-year Data Set. Note that the spatial coordinate axis of DE436 is defined by the International Celestial Reference System (ICRS). The BCRS and the GCRS do not rotate with respect to ICRS.

[3)] https://www.bipm.org/en/bipm-services/timescales/time-ftp/Circular-T.html
[4)] http://hpiers.obspm.fr/eoppc/bul/bulc/UTC-TAI.history
[5)] https://www.bipm.org/en/bipm-services/timescales/time-ftp/ttbipm.html

We also need the vector from the geocenter to the observatory on the Earth's surface. This means that we need to know the relationship between the GSRS and the coordinate system that rotates with the Earth. The time scale to know the rotation of the Earth is UT1, and the relationship between UT1 and UTC is provided by the Bulletin B of the IERS.[6)] The orientation of the coordinate system rotating with the Earth has the following three effects: precession and nutation, Earth's spin rotation, and polar motion. When creating a residual with TEMPO2, these three effects can be included, but a model that ignores polar motion is used in NANOgrav 11-year Data Set.

3.2.2 Solar system delay

In this section we describes the delays caused in the solar system. There are four main sources of the delay: the general coordinate transformation from the GCRS to the BCRS (Einstein delay), the difference of TOA between the observatory and the SSB, which is emitted at the same time (Roemer delay and parallax), the gravitational potential of the solar system objects (Shapiro delay). The equation can be written as

$$\Delta_{\odot} = \Delta_{\mathrm{E}} + \Delta_{\mathrm{R}} + \Delta_{\mathrm{p}} + \Delta_{\mathrm{S}}. \tag{3.2.3}$$

Einstein delay

The Einstein delay occurs when transforming from TCG to TCB. This delay is purely the effect of a general coordinate transformation from GCRS to BCRS. For metric and transformation of the GCRS and the BCRS, see the IAU Resolutions Adopted at the XXIVth General Assembly.[7)] The Einstein delay Δ_{E} can be written as follows:

$$\Delta_{\mathrm{E}} = TCB - TCG = \frac{1}{c^2}\left(\int_{t_0}^{t}\left(\frac{|\mathbf{v}_{\mathrm{E}}|^2}{2} + U_{\mathrm{ext}}(\mathbf{r}_{\mathrm{E}})\right)dt + \mathbf{v}_{\mathrm{E}}\cdot(\mathbf{r}_{\mathrm{o}} - \mathbf{r}_{\mathrm{E}})\right), \tag{3.2.4}$$

where $\mathbf{r}_{\mathrm{E}}$ and $\mathbf{v}_{\mathrm{E}}$ are the position and the velocity of the geocenter with respect to the BCRS, $\mathbf{r}_{\mathrm{o}}$ is the position of the observatory with respect to the BCRS, and $U_{\mathrm{ext}}(\mathbf{r}_{\mathrm{E}})$ is the potential of the solar system objects except for the Earth. In TEMPO2, two methods of articles [28, 26] can be used for integration of the first term. The methods of the article [28] is used in the NANOgrav 11-year Data Set.

Røemer delay and parallax

The Røemer delay is the difference in the TOA between the geocenter and the SSB. The pulse is assumed to propagate in the vacuum and the wavefront is a plane. The Røemer delay Δ_{R} simply can be written as follows:

$$\Delta_{\mathrm{R}} = -\frac{\mathbf{r}_{\mathrm{o}}\cdot\hat{\mathbf{R}}}{c}, \tag{3.2.5}$$

[6)] http://hpiers.obspm.fr/iers/bul/bulb_new/

[7)] https://www.iers.org/SharedDocs/Publikationen/EN/IERS/Publications/tn/TechnNote32/tn32_117.pdf?__blob=publicationFile&v=1

where $\hat{\mathbf{R}}$ the unit vector for the position of the pulsar barycenter (if binary, binary barycenter) with respect to the BCRS. Since it takes 500s for the light to travel from the sun to the earth, the Røemer delay is the largest delay among the solar system delays. Due to the revolution of the Earth, the Røemer delay has an oscillation component of one year cycle.

The Røemer delay assumes that the pulse wavefront is a plane, but the actual pulse wavefront is a sphere. The parallax is introduced to take into account that the wavefront of the pulse is a sphere. Assuming that the distance between the Earth and the pulsar is very long compared to the revolution radius of the Earth, the parallax can be written as follows [29]:

$$\Delta_{\mathrm{p}} = \frac{|\mathbf{r}_{\mathrm{o}\perp}|^2}{2cd_{\mathrm{p}}}, \tag{3.2.6}$$

where $\mathbf{r}_{\mathrm{o}\perp} \equiv \mathbf{r}_{\mathrm{o}} - \mathbf{r}_{\mathrm{o}\|} \cdot \hat{\mathbf{R}}_0$, $\mathbf{x}_{\mathrm{o}\|} \equiv \mathbf{r}_{\mathrm{o}} \cdot \hat{\mathbf{R}}_0$, $\hat{\mathbf{R}}_0$ is the $\hat{\mathbf{R}}$ at a given epoch, and d_{p} is the distance from the Earth and the pulsar. Due to the revolution of the earth, the parallax has an oscillation component of half a year cycle.

Shapiro delay

The Shapiro delay occurs when a pulse passes through the gravitational potential of the solar system objects. Under the weak field approximation, the Shapiro delay can be written as follows [30, 31]:

$$\Delta_{\mathrm{S}} = -2\sum_{A} \frac{GM_A}{c^3} \ln(\hat{\mathbf{R}} \cdot \mathbf{r}_A + |\mathbf{r}_A|), \tag{3.2.7}$$

where A is a subscript for the solar system object to be considered, M_A is the mass of the solar system object A, and $\mathbf{r}_A$ is the vector from the solar system object A to the observatory. that Shapiro delay is always negative. The solar system object that contributes most to the Shapiro delay is the sun. In TEMPO2, in addition to the sun, planets can be included in Eq. (3.2.7). Only the sun is used in the NANOgrav 11-year Data Set.

3.2.3 Interstellar delay

The interstellar delay is caused by a pulse passing through the interstellar plasma. In the plasma, the group velocity of the light changes from that in the vacuum. As a characteristic of the Interstellar delay, the delay depends on the light frequency. Therefore, the interstellar delay can be examined by observing light with different frequencies. The interstellar delay is expressed by two component: the delay induced by the integrated column density of the electrons (Dispersion measure, DM), and the additional delay depends on light frequency (Frequency Dependent delay, FD). The equation can be written as

$$\Delta_{\mathrm{IS}} = \Delta_{\mathrm{DM}} + \Delta_{\mathrm{FD}}. \tag{3.2.8}$$

Interstellar dispersion delay

The integrated column density of electrons is called dispersion measure:

$$\mathrm{DM} = \int_0^L n_e d\ell, \tag{3.2.9}$$

where n_e is the electron number density, and L is the distance from the Earth to the pulsar. Then, Interstellar dispersion delay can be written as follows [31]:

$$\Delta_{\mathrm{DM}} = \frac{1}{f_{\mathrm{SSB}}^2} \frac{e^2}{2\pi m_e c} \mathrm{DM}, \tag{3.2.10}$$

$$f_{\mathrm{SSB}} = \left(1 + \frac{d\Delta_{\mathrm{R}}}{dt}\right) f, \tag{3.2.11}$$

where e is the electron charge, m_e is the electron mass, and $d\Delta_{\mathrm{R}}/dt$ is the redshift due to the Røemer delay. Interstellar dispersion delay is known to have temporal variations. This variation would be caused by the variation of the electron density and by the pulsar motion. The time variation of the DM is calculated for each pulsar observation in the NANOGrav.

Frequency Dependent delay

It is known that the pulse shape varies depending on the frequency of the pulse [32]. To characterize this variation, the FD delay was introduced:

$$\Delta_{\mathrm{FD}} = \sum_i^n c_i \log\left(\frac{f_{\mathrm{SSB}}}{1\mathrm{GHz}}\right)^i, \tag{3.2.12}$$

where c_i is the fitting parameter, and the n is increased until the FD delay is sufficiently low.

3.2.4 Binary delay

Binary delay occurs when the millisecond pulsar is a binary. Many binary models are considered in the pulsar timing. For example, the Damour and Deruelle (DD) model [33] can be used in post-newtonian situations. The T2 model based on the DD model, unlike the DD model, can be used in the case of two or more companions. In addition, the ELL1 model [34] is numerically more stable than other models for binaries with a low eccentricity. Since the binary orbital period would be on the order of days, it is considered that the main component of the oscillation is sufficiently higher than the region of our interest.

3.2.5 Uncertainty of fitting in timing model

There is always uncertainty in parameter fitting. The uncertainty of fitting in timing model would be written as

$$\delta\tau = t_{\rm obs} - t_{\rm det}(\xi_{\rm est}) = t_{\rm det}(\xi_{\rm true}) - t_{\rm det}(\xi_{\rm est}) + n, \tag{3.2.13}$$

where $t_{\rm det}$ is the timing model, $\xi_{\rm est}$ is the estimated parameters, $\xi_{\rm true}$ is the true parameter values, and n is the noise which is not included in timing model. We assume that the estimated parameters can be written with uncertainty ϵ and the true parameter values. Then assuming the estimated parameters is very close to the true parameter values, the residual becomes

$$\begin{aligned}
\delta\tau &= t_{\rm det}(\xi_{\rm est}+\epsilon) - t_{\rm det}(\xi_{\rm est}) + n \\
&= \left.\frac{\partial t_{\rm det}(\xi_{\rm est}+\epsilon)}{\partial\xi}\right|_{\epsilon=0} \epsilon + n + \mathcal{O}(\epsilon^2) \\
&= M\epsilon + n + \mathcal{O}(\epsilon^2), \\
M &\equiv \left.\frac{\partial t_{\rm det}(\xi_{\rm est}+\epsilon)}{\partial\xi}\right|_{\epsilon=0},
\end{aligned} \tag{3.2.14}$$

where M is called the design matrix whose columns correspond to the linearized (around the estimated timing parameters) timing model.

There is uncertainty of fitting in timing model is used in our analysis. Therefore we should explain the nature of the design matrix. Figure 3.2 is a plot of the design matrix for PSR J1713+0747. As you can see, the spin-down parameters are large below 10^{-8}Hz. We are interested in frequencies below 10^{-8}Hz, so that there is a decrease in sensitivity due to the spin-down parameters.

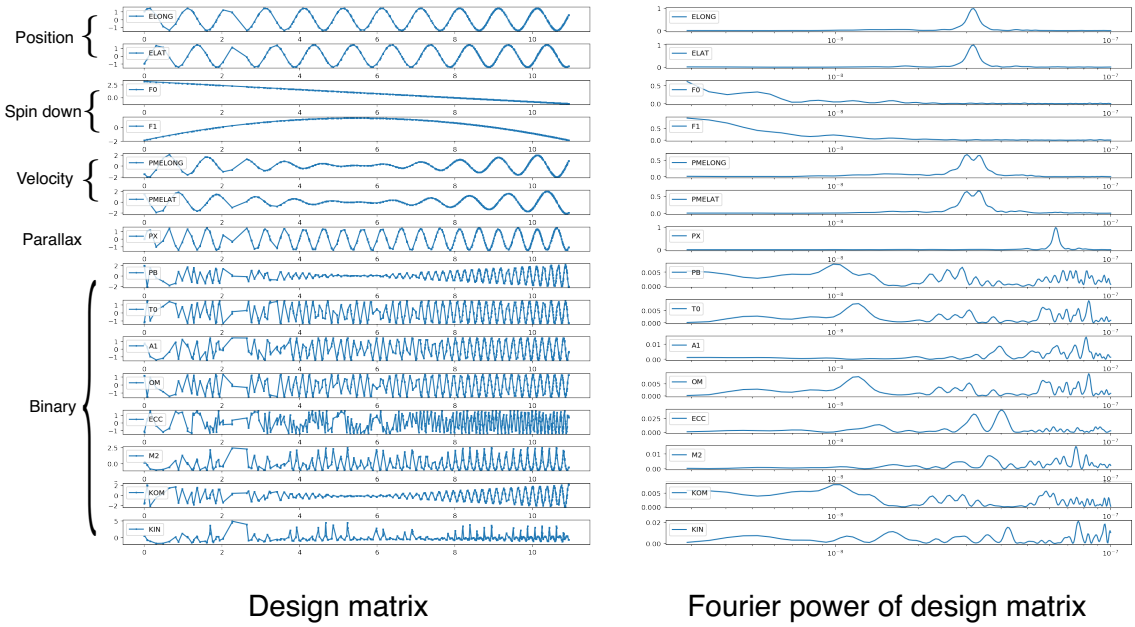

Figure 3.2: Left: Plot of the normalized design matrix. Right: Plot of the Fourier power of the normalized design matrix.

Chapter 4

Bayesian analysis in the time domain

In this chapter, we explain the data D, the model $\mathcal{M}$, and the parameter θ used in Bayesian analysis, and define the posterior probability distribution $p(\theta|D, \mathcal{M})$, the likelihood function $p(D|\theta, \mathcal{M})$, and the prior probability distribution $p(\theta|\mathcal{M})$. For the review of the Bayesian parameter estimation and model comparison, see the Appendix A.

4.1 Data

We used the NANOGrav 11-year data set [35] and chose six pulsars: PSRs J0613-0200, J1012+5307, J1600-3053, J1713+0747, J1744-1134, and J1909-3744. In this dataset, these pulsars have relatively good time-of-arrival (TOA) precision and long observation time, which would be suitable for detecting the signal of the FDM which becomes larger as the frequency becomes lower.

The data D we use for the Bayesian analysis are timing residuals which are calculated by subtracting the timing model from the TOAs. The fitting to make timing residual is called timing fit, which removes the currently well-known effects. The parameters included in the timing model are spin parameters, astrometry parameters, binary parameters (if pulser is binary), dispersion measure parameters, frequency dependency parameters, jump parameters, see the articles [32, 35] for details. Inaccuracies in the timing fit are taken into account by the TM noise in Section 4.3. Note that, by fitting the spin parameters, some of the low frequency signal that we are searching for in this thesis will be absorbed [36, 37]. In the timing fit, TT (BIPM2015)[1)] is used for the Terrestrial Time, and JPL DE436 [27] is used for the planetary ephemeris. It is known that the timing residuals change greatly depending on which planetary ephemeris is selected. To account for this error, the SSE noise described in Section 4.3 was first introduced to the model by the article [38].

[1)] https://www.bipm.org/en/bipm-services/timescales/time-ftp/ttbipm.html

In order to obtain the timing residuals, we use the libstempo[2)] which is the PYTHON interface to TEMPO2.[3)] For the parameter files which include the timing model parameters and for timing files which include TOAs and the uncertainties of TOAs, we used the identical data set except for the parameter file of PSR J1713+0747. In the parameter file of the PSR J1713+0747, we changed only a parameter EPHEM from DE430 [39] to DE436, where this parameter specifies which ephemerides to be used. Then we used libstempo to fit the timing parameters of the PSR J1713+0747 and created a new parameter file. We verified that change in ephemeris did not make much difference to the timing parameters.[4)] We iterated the parameter fitting five times, which would be sufficient for parameters to converge to certain values. All of our Bayesian analysis was done using this new parameter file of the PSR J1713+0747.

4.2 Signal

The parameters used in the Bayesian estimation are defined as follows:

$$s(t) = -\frac{\Psi}{2\pi f}[\sin(2\pi f t + \alpha_e) - \sin(2\pi f t + \alpha_p)], \tag{4.2.1}$$

where we auumed $\Psi \equiv \Psi(\mathbf{x_e}) = \Psi(\mathbf{x_p})$ and defined

$$\alpha_e \equiv 2\alpha(\mathbf{x_e}), \quad \alpha_p \equiv 2\alpha(\mathbf{x_p}) - 2\pi f D \ . \tag{4.2.2}$$

Here, since we do not aim to estimate the distance, we put together the phase $\alpha(\mathbf{x_p})$ and the distance D. In fact, the distance has an uncertainty of tens to hundreds of parsec currently that is too large to determine the phase [35]. Since, as is mentioned in the article [11], the distance between the Earth and the pulsar D is not so large, it is reasonable to assume that the amplitudes at the earth $\Psi(\mathbf{x_e})$ and the pulsar $\Psi(\mathbf{x_p})$ are equal. Note that the overall sign of Eq. (4.2.1) only changes the definition of phase and does not affect the analysis that limits the amplitude.

Assuming that the FDM occupies all of the dark matter energy density, we have

$$\begin{aligned} \Psi &\simeq 6.48 \times 10^{-16} \left(\frac{\rho}{0.4\mathrm{Gev/cm}^3}\right) \left(\frac{10^{-23}\mathrm{eV}}{m}\right)^2, \\ &\simeq 9.47 \times 10^{-16} \left(\frac{\rho}{0.4\mathrm{Gev/cm}^3}\right) \left(\frac{4 \times 10^{-9}\mathrm{Hz}}{f}\right)^2, \end{aligned} \tag{4.2.3}$$

[2)] http://vallis.github.io/libstempo

[3)] We confirmed that each pulsar's value of the chi-square and the degrees of freedom which can be derived by TEMPO2 are consistent with values listed in the file 'stats_11y_20180226.dat', where this file is included in the data set and can be used as to see if TEMPO2 is properly constructed. Therefore, TEMPO2 was installed as expected.

[4)] We found that the LAMBDA and BETA parameters of the astrometry parameters shift by more than one sigma away from the older value. This result can be inferred from the deviation of the position parameter due to the difference in ephemeris as pointed out in the article [40].

and

$$f \simeq 4.84 \times 10^{-9}\mathrm{Hz}\left(\frac{m}{10^{-23}\mathrm{eV}}\right), \tag{4.2.4}$$

where $\rho = 0.4\mathrm{Gev/cm}^3$ is the estimated energy density of the dark matter at the position of the Earth [41].

4.3 Model

Following the paper [32, 38], the timing residuals $\delta\boldsymbol{t}$ for each pulsar can be written as follows

$$\delta\boldsymbol{t} = \boldsymbol{s} + \boldsymbol{n}_{\mathrm{TM}} + \boldsymbol{n}_{\mathrm{red}} + \boldsymbol{n}_{\mathrm{SSE}} + \boldsymbol{n}_{\mathrm{white}}, \tag{4.3.1}$$

where these variables are N_{TOA} dimensional vectors and N_{TOA} denotes the number of TOAs of the pulsar. In the Bayesian framework, Eq. (4.3.1) is the model $\mathcal{M}$ for the residuals $\delta\boldsymbol{t}$ which are the data D. Each term on the right-hand side is described below. The first term on the right-hand side $\boldsymbol{s}$ is the FDM signal, which is given by Eq. (4.2.1). The second term $\boldsymbol{n}_{\mathrm{TM}}$ is the noise due to inaccuracies of the timing model, which is represented by

$$\boldsymbol{n}_{\mathrm{TM}} = \boldsymbol{M}\boldsymbol{\epsilon}. \tag{4.3.2}$$

$\boldsymbol{M}$ is a $N_{\mathrm{TOA}} \times N_{\mathrm{TM}}$ design matrix whose rows describe the dependence of the pulsar timing residuals on respective timing model parameters, where N_{TM} is the number of the timing model parameters. $\boldsymbol{\epsilon}$ is a N_{TM} dimensional vector, which denotes small offset for the timing model parameters. We will refer to this noise as the TM noise. We obtain the design matrix using the TEMPO2 via libstempo, and the timing model parameters used are listed in [35].

The third term $\boldsymbol{n}_{\mathrm{red}}$ is the red noise for which the power spectral density has most of their power at low frequencies in a given data set. The red noise is known to have achromatic (observing-frequency-independent) and chromatic (observing-frequency-dependent) components [42]. The achromatic components are thought to be caused by a random walk in one of the pulsar spin parameters [43, 44, 45, 46] and contributions to TOAs by an asteroid belt around the pulsar [47]. The chromatic components are thought to be caused by the pulse propagating through the ionized interstellar medium if the dispersion measure of the timing model does not describe all this effect [35]. This components therefore would be induced either by diffractive and refractive interstellar effects [48, 42] not included in the timing model or by unmodeled propagation effects. Although the origins of red noise are various, simple power-law spectrum form is often used as the power spectral density. Under the assumption of the stationary Gaussian process, the power spectral density $P(f)$ can be written as

$$P(f) = \frac{A_{\mathrm{red}}^2}{12\pi^2}\left(\frac{f}{f_{\mathrm{yr}}}\right)^{3-\gamma_{\mathrm{red}}} f^{-3}, \tag{4.3.3}$$

where f is a red noise frequency, $f_{\rm yr}$ is $1{\rm yr}^{-1}$, $A_{\rm red}$ is a dimensionless amplitude of the red noise, and $\gamma_{\rm red}$ is a spectral index of the red noise. Note that this parameterization is the analogy of the power-law model for the stochastic gravitational wave background [49, 50]. In order to improve computational efficiency, the red noise was described by the Fourier series rather than by analytical solution of the covariance matrix calculated from the power spectral density Eq. (4.3.3) [51, 52, 53]. In particular, by defining red noise with Fourier series expansion, it is possible to use TM noise and red noise in a unified description when analytical marginalization of the posterior probability distribution is performed [32, 54]. We use the same formulation in the next section. Therefore, the red noise in component form is defined as

$$n_{{\rm red},i} = \sum_{j=1}^{N_{\rm red}} \left[a_j \cos\left(\frac{2\pi j t_i}{T}\right) + b_j \sin\left(\frac{2\pi j t_i}{T}\right)\right], \tag{4.3.4}$$

where $n_{{\rm red},i}$ is the red noise at the t_i which is $i^{\rm th}$ TOA, a_j and b_j are the the Fourier series coefficients, $N_{\rm red}$ is a number of frequencies used, T is the total observation time span which is unique for each pulsar. Then like the second term $\boldsymbol{n}_{\rm TM}$, the red noise is represented by

$$\boldsymbol{n}_{\rm red} = \boldsymbol{F}\boldsymbol{a} \tag{4.3.5}$$

where $\boldsymbol{F}$ is a $N_{\rm TOA} \times 2N_{\rm red}$ matrix which has columns of alternating cosine and sine functions, and $\boldsymbol{a}$ is a $2N_{\rm red}$ dimensional vector which has coefficients corresponding to cosine and sine functions, that is, in a component form,

$$F_{ik} = \begin{cases} \cos\left(\frac{2\pi k t_i}{T}\right), & (k = odd) \\ \sin\left(\frac{2\pi (k-1) t_i}{T}\right), & (k = even) \end{cases}, \quad a_k = \begin{cases} a_k, & (k = odd) \\ b_{k-1}, & (k = even) \end{cases}, \tag{4.3.6}$$

where k is the number from 1 to $2N_{\rm red}$. Assuming the independence of each Fourier series coefficient, the relation between Fourier series coefficients and power spectral density Eq. (4.3.3) is defined as

$$\begin{aligned} \langle a_k a_{k'} \rangle &= \begin{cases} P\left(\frac{k}{T}\right) \Delta f \delta_{k,k'}, & (k = odd) \\ P\left(\frac{k-1}{T}\right) \Delta f \delta_{k,k'}, & (k = even) \end{cases} \\ &\equiv \Xi_k \end{aligned} \tag{4.3.7}$$

where $< \ldots >$ denotes an ensemble average, Δf is a frequency resolution, which is about $1/T$, and $\delta_{k,k'}$ is the Kronecker delta. With this expression, the relation between the cross-correlation function of red noise $C_{\rm red}$ and the power spectral density is given by

$$C_{{\rm red},i,i'} = \langle n_{{\rm red},i} n_{{\rm red},i} \rangle = \sum_{k}^{2N_{\rm red}} \sum_{k'}^{2N_{\rm red}} F_{i,k} \langle a_k a_{k'} \rangle F_{i',k'} = \sum_{j}^{N_{\rm red}} P\left(\frac{j}{T}\right) \cos\left(\frac{2\pi j (t_i - t_{i'})}{T}\right) \Delta f. \tag{4.3.8}$$

This relation is expected from the Wiener-Khinchin theorem for the stationary process. In this thesis we use $N_{\rm red} = 30$. If $N_{\rm red}$ is set to 30, then the maximum frequency $30/T$ is about 10^{-7}Hz, because the total observation time span T is 11 years. Thus, $N = 30$ is sufficient to describe the red noise that increases below 10^{-8}Hz.

The fourth term $n_{\rm SSE}$ is a noise due to inaccuracies of a Solar System ephemeris (SSE) which is used to convert the TOAs at the geocenter to those at the Solar System barycenter (SSB). We will refer to this noise as the SSE noise. It is known that SSE errors affect upper limits and Bayes factors for amplitudes of the stochastic gravitational wave background [38]. The stochastic gravitational wave background can be distinguished from the SSE errors by using the two-point correlation analysis in principle [55], on the other hand the FDM signal cannot be distinguished from the SSE errors using the correlation analysis, because the correlation function characterizing the FDM signal is not defined. Therefore, the presence of the SSE errors would have a stronger influence on the analysis of the FDM signal than in the case of the stochastic gravitational wave background. Following [38], we assume that the SSE errors only affect the Rømer delay $\Delta_{\rm R}$ which is the vacuum light travel time between the geocenter and the SSB. Therefore, the Rømer delay at the t_i is

$$\Delta_{{\rm R},i} = \boldsymbol{r}_i \cdot \boldsymbol{R}_i, \tag{4.3.9}$$

where $\boldsymbol{r}_i$ is the vector from the geocenter to the SSB, and $\boldsymbol{R}_i$ is the unit vector from the SSB to the pulsar barycenter [23]. In the case that the position shift of the SSB is induced by the error of the planet mass from the SSE, this shift changes the vector $\boldsymbol{r}_i$, so that the induced residuals $n^{mass}_{{\rm SSE},i}$ at the t_i can be written as [56]

$$n^{\rm mass}_{{\rm SSE},i} = -\delta M(\boldsymbol{b}_i \cdot \boldsymbol{R}_i), \tag{4.3.10}$$

where δM is the error of the planet mass in solar mass $M_\odot$ unit and $\boldsymbol{b}_i$ is the vector from the planet barycenter to the SSB. The planets we consider the error of mass are Jupiter, Saturn, Uranus, and Neptune. As in the above case, the error of the planet orbit from the SSE induce the residuals $n^{orbit}_{{\rm SSE},i}$

$$n^{\rm orbit}_{{\rm SSE},i} = -M\left(\sum_{\mu}^{6} \frac{\partial \boldsymbol{b}_i}{\partial a_\mu}\delta a_\mu\right) \cdot \boldsymbol{R}_i, \tag{4.3.11}$$

where M is the planet mass in solar mass unit, a_μ are set-III parameters [57] which are composed of six parameters and characterize an osculating elliptical orbit at a given osculation epoch, and δa_μ are small offsets of the set-III parameters. We have to consider the error of the orbit of Jupiter. We also consider a rotation of the vector $\boldsymbol{r}_i$ around the ecliptic pole,

$$\begin{aligned} n^{\rm rotation}_{{\rm SSE},I} &= (\boldsymbol{r}_i - R_z(\theta)\boldsymbol{r}_i) \cdot \boldsymbol{R}_i, \\ R_z(\theta) &\equiv \begin{pmatrix} \cos\theta & -\sin\theta & 0 \\ \sin\theta & \cos\theta & 0 \\ 0 & 0 & 1 \end{pmatrix}, \quad \theta \equiv \delta z \frac{\rm second}{\rm year}(t_i - t_0) \end{aligned} \tag{4.3.12}$$

where $R_z(\theta)$ is a rotation matrix, δz is a rotation rate which has the unit rad/year, and t_0 is the offset of time. Among the noises mentioned above, the dominant contribution to the residuals comes from Jupiter, because Jupiter has a large mass and is thought to have a relatively large orbital error compared to Saturn [58]. Uranus and Neptune also have large uncertainty, but the orbital periods are sufficiently longer than the observation time of pulsars, hence the induced residuals are proportional to the time and absorbed by fitting of timing model for the intrinsic pulsar spin periods [36, 37]. Thus, the noise due to inaccuracies of the SSE reads

$$\boldsymbol{n}_{\rm SSE} = \boldsymbol{n}_{\rm SSE}^{\rm mass,J} + \boldsymbol{n}_{\rm SSE}^{\rm mass,S} + \boldsymbol{n}_{\rm SSE}^{\rm mass,U} + \boldsymbol{n}_{\rm SSE}^{\rm mass,N} + \boldsymbol{n}_{\rm SSE}^{\rm orbit,J} + \boldsymbol{n}_{\rm SSE}^{\rm rotation}, \tag{4.3.13}$$

where $\boldsymbol{n}_{\rm SSE}^{\rm mass,J}, \boldsymbol{n}_{\rm SSE}^{\rm mass,S}, \boldsymbol{n}_{\rm SSE}^{\rm mass,U}, \boldsymbol{n}_{{\rm SSE},i}^{\rm mass,N}$ are the noises due to the mass errors of Jupiter, Saturn, Uranus, and Neptune, respectively, $\boldsymbol{n}_{{\rm SSE},i}^{\rm orbit,J}$ is the noise due to the orbit errors of Jupiter, and $\boldsymbol{n}_{\rm SSE}^{\rm rotation}$ is the noise due to the rotation rate around the ecliptic pole. We used the values and the data implemented in ENTERPRISE (Enhanced Numerical Toolbox Enabling a Robust PulsaR Inference SuitE) which is a pulsar timing analysis code[5)]. Thus, the value of the Jupiter's mass M^J is the value of the IAU 2009 system of astronomical constants [59] and the value of t_0 corresponds to MJD 55197, and the data of $\partial \boldsymbol{b}_i/\partial a_\mu$ are the same in ENTERPRISE. Note that, in the data of $\partial \boldsymbol{b}_i/\partial a_\mu$, the principal component analysis (PCA) was performed for six $\partial \boldsymbol{b}_i/\partial a_\mu$, so that small offsets δa_μ do not correspond to the set-III parameters a_μ themselves but correspond to parameters based on PCA bases. In the calculation of the shifted $\boldsymbol{r}_i$ due to the SSE errors, to reduce the $N_{\rm TOA}$ for efficient computation, $\boldsymbol{b}_i$ and $\boldsymbol{r}_i$ are averaged within the TOAs obtained in one observation at one combination of receivers and backend systems, and the data of $\partial \boldsymbol{b}_i/\partial a_\mu$ are interpolated into the corresponding averaged TOAs.[6)] After that, assuming the value of SSE noise is same within the TOAs obtained in one observation at one combination of receivers and backend systems, the shift of $\boldsymbol{r}_i$ due to the SSE errors is calculated. We obtained the unit vector from the SSB to the pulsar barycenter $\boldsymbol{R}_i$ using the TEMPO2 via the libstempo.

The last term $\boldsymbol{n}_{\rm white}$ is roughly called as a white noise. Assuming that this noise follows the Gaussian distribution, we characterize it by a correlation function:

$$\boldsymbol{C}_{\rm white} = \left\langle \boldsymbol{n}_{\rm white} \boldsymbol{n}_{\rm white}^T \right\rangle = \boldsymbol{C}_{\rm EFAC} + \boldsymbol{C}_{\rm EQUAD} + \boldsymbol{C}_{\rm Jitter}, \tag{4.3.14}$$

where $\boldsymbol{C}_{\rm EFAC}$, $\boldsymbol{C}_{\rm EQUAD}$, and $\boldsymbol{C}_{\rm ECORR}$ are correlation functions for EFAC, EQUAD, and ECORR parameters, respectively. Each term on the right-hand side is described below. When sorting TOAs by what combination of receivers and backend systems were used,

[5)] https://github.com/nanograv/enterprise

[6)] In the pulsar we used, we confirmed that there was no overlap between each observation of receivers and backend systems. Therefore, each observation can be divided appropriately.

the first term $\boldsymbol{C}_{\mathrm{EFAC}}$ can be written as follows:

$$\boldsymbol{C}_{\mathrm{EFAC}} = \begin{pmatrix} e_1^2\boldsymbol{W}_1 & & & 0 \\ & e_2^2\boldsymbol{W}_2 & & \\ & & \ddots & \\ 0 & & & e_{N_{back}}^2\boldsymbol{W}_{N_{back}} \end{pmatrix}, \tag{4.3.15}$$

where N_{back} denotes the number of the combinations of receivers and backend systems, a is the subscript for N_{back}, e_a is called as a EFAC parameter, $\boldsymbol{W}_a$ is a $N_{\mathrm{TOA}_a} \times N_{\mathrm{TOA}_a}$ diagonal matrix composed of TOA measurement uncertainties obtained by the ath combination, and N_{TOA_a} denotes the number of the TOAs obtained by the ath combination. From the above equation, it can be seen that EFAC parameters depend on the ath combination and changes the size of the error bars of TOAs. This noise characterize systematic errors of TOA measurement uncertainties. As in the case of the EFAC parameters, the second term $\boldsymbol{C}_{\mathrm{EQUAD}}$ can be written as follows:

$$\boldsymbol{C}_{\mathrm{EQUAD}} = \begin{pmatrix} q_1^2\boldsymbol{I}_1 & & & 0 \\ & q_2^2\boldsymbol{I}_2 & & \\ & & \ddots & \\ 0 & & & q_{N_{back}}^2\boldsymbol{I}_{N_{back}} \end{pmatrix}, \tag{4.3.16}$$

where q_a is the EQUAD parameter and I_a is the $N_{\mathrm{TOA}_a} \times N_{\mathrm{TOA}_a}$ identity matrix. This noise is an additional white Gaussian noise. When sorting TOAs in the order of observation for each combination separately, the last term $\boldsymbol{C}_{\mathrm{ECORR}}$ can be written as follows:

$$\begin{aligned} \boldsymbol{C}_{\mathrm{ECORR}} &= \begin{pmatrix} \boldsymbol{J}_1 & & & 0 \\ & \boldsymbol{J}_2 & & \\ & & \ddots & \\ 0 & & & \boldsymbol{J}_{N_{back}} \end{pmatrix}, \\ \boldsymbol{J}_a &\equiv \begin{pmatrix} \boldsymbol{u}_{a1}j_a^2\boldsymbol{u}_{a1}^T & & & 0 \\ & \boldsymbol{u}_{a2}j_a^2\boldsymbol{u}_{a2}^T & & \\ & & \ddots & \\ 0 & & & \boldsymbol{u}_{aN_{obs,a}}j_a^2\boldsymbol{u}_{aN_{obs,a}}^T \end{pmatrix}, \\ \boldsymbol{u}_{ab} &\equiv \left.\begin{pmatrix} 1 \\ 1 \\ \vdots \\ 1 \end{pmatrix}\right\} N_{\mathrm{TOA}_{ab}}, \end{aligned} \tag{4.3.17}$$

where $N_{obs,a}$ denotes the number of the observation using the ath combination, b is the subscript for $N_{obs,a}$, j_a is the ECORR parameter, $\boldsymbol{u}_{ab}$ is the $N_{\text{TOA}_{ab}}$ dimensional vector of which all the components are one, and $N_{\text{TOA}_{ab}}$ denotes the number of the TOAs obtained within the bth observation using the ath combination. This noise shows that there is a correlation between the TOAs obtained during one observation and there is no correlation between the TOAs obtained by other observations. This noise characterizes pulse jitter caused by stochastic amplitude and phase variations in pulse, which correlates in a certain frequency band and doesn't correlate in time [48].

To summarize, the parameters θ for the Bayesian data analysis are Ψ, f, α_e, and α_p of the FDM signal, $\boldsymbol{\epsilon}$ of the TM noise, $\boldsymbol{a}$ of the red noise, $\delta M, \delta a_\mu$, and δz of the SSE noise, and e_a, q_a, and j_a of the white noise. Note that the parameters $\Psi, f, \alpha_e, \delta M, \delta a_\mu$, and δz are common to all pulsars. The red noise defined in this section is the hierarchical model in the Bayesian framework, and A_{red} and γ_{red} are called hyperparameters which are the parameters of the parameter $\boldsymbol{a}$. In addition, the TM noise defined in this section is not the hierarchical model, but it is defined in the same way as the red noise. Therefore the parameters $\boldsymbol{\epsilon}$ of the TM noise follow the Gaussian distribution, and the variance-covariance matrix in component form becomes as follows:

$$\langle \epsilon_l \epsilon_{l'} \rangle = \Phi_l \delta_{l,l'}, \tag{4.3.18}$$

where l is the subscript for N_{TM}, and Φ_l are the hyperparameters which are the parameter of the parameter ϵ_l. The reason for doing this is to use the TM noise and the red noise in a unified description as mentioned in the explanation of red noise. Then, we can avoid problems in marginalizing the posterior probability distribution with uniform prior.

4.4 Likelihood Function and Posterior Probability Distribution

In this section we derive the likelihood function and the posterior probability distribution used in the Bayesian estimation. We basically follow the article [38].

If the model $\mathcal{M}$ for the data D is given, the likelihood function $p(D|\theta, \mathcal{M})$ can be obtained. In the model $\mathcal{M}$ for the residuals $\delta\boldsymbol{t}$ given by Eq. (4.3.1) , the white noise has the statistical uncertainty, on the other hand, the others are determined by given parameters.[7)] In this case, since the white noise has the Gaussian distribution, the

[7)] The statistical uncertainty of the TM noise and the red noise are parametrized by not the parameter but the hyperparameter. Therefore, as can be seen from Eq. (1.0.6), when constructing a likelihood function, the TM noise and the red noise are determined by given parameters.

likelihood for each pulsar can be written as [60]

$$
\begin{aligned}
&p(\delta\boldsymbol{t}|\boldsymbol{\theta},\mathcal{M}) \\
&= \frac{1}{\sqrt{\det(2\pi\boldsymbol{C}_{\rm white})}} \\
&\times\exp\left(-\frac{1}{2}\left(\delta\boldsymbol{t}-\boldsymbol{s}-\boldsymbol{n}_{\rm TM}-\boldsymbol{n}_{\rm red}-\boldsymbol{n}_{\rm SSE}\right)^T\boldsymbol{C}_{\rm white}^{-1}\left(\delta\boldsymbol{t}-\boldsymbol{s}-\boldsymbol{n}_{\rm TM}-\boldsymbol{n}_{\rm red}-\boldsymbol{n}_{\rm SSE}\right)\right).
\end{aligned}
\tag{4.4.1}
$$

The likelihood function for all pulsars can be written by multiplying the likelihood function of each pulser, because it is considered that there is no correlation between the residuals of each pulsar. If one wants to estimate all the parameters, one can use this likelihood function.

In most cases in analyses with PTAs, the parameters $\boldsymbol{\epsilon}$ of the TM noise and the parameters $\boldsymbol{a}$ of the red noise are eliminated by marginalizing the posterior probability distribution before analyzing the data. Since the parameters $\boldsymbol{\epsilon}$ and $\boldsymbol{a}$ are unique to each pulsar, the marginalization can be done independently for each pulsar, we can calculate the posterior probability distribution in the case of a single pulsar. Our formulation of the marginalization is the same as that in the papers [32, 54]. Following these papers, the likelihood function Eq. (4.4.1) is rewritten as

$$
\begin{aligned}
p(\delta\boldsymbol{t}|\boldsymbol{\theta},\mathcal{M}) &= \frac{1}{\sqrt{\det(2\pi\boldsymbol{C}_{\rm white})}}\exp\left(-\frac{1}{2}\left(\delta\boldsymbol{r}-\boldsymbol{T}\boldsymbol{b}\right)^T\boldsymbol{C}_{\rm white}^{-1}\left(\delta\boldsymbol{r}-\boldsymbol{T}\boldsymbol{b}\right)\right), \\
\delta\boldsymbol{r} &\equiv \delta\boldsymbol{t}-\boldsymbol{s}-\boldsymbol{n}_{\rm SSE}, \\
\boldsymbol{T} &\equiv (\boldsymbol{M}\ \boldsymbol{F}), \\
\boldsymbol{b} &\equiv \begin{pmatrix}\boldsymbol{\epsilon}\\ \boldsymbol{a}\end{pmatrix},
\end{aligned}
\tag{4.4.2}
$$

where $\delta\boldsymbol{r}$ is defined only for simplifying notation, $\boldsymbol{T}$ is the $N_{\rm TOA}\times(N_{\rm TM}+2N_{\rm red})$ matrix in which the matrices $\boldsymbol{M}$ and $\boldsymbol{F}$ are concatenated along the row axis, and $\boldsymbol{b}$ is $N_{\rm TM}+2N_{\rm red}$ dimensional vector in which $\boldsymbol{\epsilon}$ and $\boldsymbol{a}$ are concatenated along the column axis. Since each noise was assumed to be Gaussian, the prior probability distribution for the parameter $\boldsymbol{b}$ can be obtained by using Eq. (1.0.5) as follows:

$$
\begin{aligned}
p(\boldsymbol{b},\boldsymbol{\eta}|\mathcal{M}) &= p(\boldsymbol{b}|\boldsymbol{\eta},\mathcal{M})p(\boldsymbol{\eta}|\mathcal{M}) = \frac{1}{\sqrt{\det(2\pi\boldsymbol{B})}}\exp\left(-\frac{1}{2}\boldsymbol{b}^T\boldsymbol{B}^{-1}\boldsymbol{b}\right)p(\boldsymbol{\eta}|\mathcal{M}), \\
\boldsymbol{B} &\equiv \mathrm{diag}(\Phi_1,\Phi_2,\cdots\Phi_l,\Xi_1,\Xi_2,\cdots\Xi_k),
\end{aligned}
\tag{4.4.3}
$$

where $\boldsymbol{B}$ is a $(N_{\rm TM}+2N_{\rm red})\times(N_{\rm TM}+2N_{\rm red})$ diagonal matrix whose diagonal elements Φ_l and Ξ_k are defined by Eq. (4.3.18) and Eq. (4.3.7) respectively, and $\boldsymbol{\eta}$ denote the hyperparameters $\Phi_l, A_{\rm red}$, and $\gamma_{\rm red}$. Note that we assume the statistical independence of the parameters and the hyperparameters. Then, using Eq. (1.0.6), the posterior

probability distribution can be written as

$$
\begin{aligned}
p(\boldsymbol{\theta},\boldsymbol{\eta}|\delta\boldsymbol{t},\mathcal{M}) &= \frac{p(\delta\boldsymbol{t}|\boldsymbol{\theta},\mathcal{M})p(\boldsymbol{\theta},\boldsymbol{\eta}|\mathcal{M})}{p(D|\mathcal{M})} \\
&= \frac{p(\delta\boldsymbol{t}|\boldsymbol{\phi},\boldsymbol{b},\mathcal{M})p(\boldsymbol{b},\boldsymbol{\eta}|\mathcal{M})p(\boldsymbol{\phi}|\mathcal{M})}{p(D|\mathcal{M})} \\
&= \frac{1}{\sqrt{(2\pi)^{N_{\rm TOA}+N_{\rm TM}+2N_{\rm red}}\det(\boldsymbol{C}_{\rm white})\det(\boldsymbol{B})}} \\
&\times \exp\left(-\frac{1}{2}\left[(\delta\boldsymbol{r}-\boldsymbol{T}\boldsymbol{b})^T\boldsymbol{C}_{\rm white}^{-1}(\delta\boldsymbol{r}-\boldsymbol{T}\boldsymbol{b})+\boldsymbol{b}^T\boldsymbol{B}^{-1}\boldsymbol{b}\right]\right) \\
&\times \frac{p(\boldsymbol{\eta}|\mathcal{M})p(\boldsymbol{\phi}|\mathcal{M})}{p(D|\mathcal{M})},
\end{aligned}
\tag{4.4.4}
$$

where $\boldsymbol{\phi}$ is the vector for all the parameters except for the parameters $\boldsymbol{b}$, which have no hyperparameters. In order to marginalize over the parameters $\boldsymbol{b}$, we performe completing the square in the exponent:

$$
\begin{aligned}
&(\delta\boldsymbol{r}-\boldsymbol{T}\boldsymbol{b})^T\boldsymbol{C}_{\rm white}^{-1}(\delta\boldsymbol{r}-\boldsymbol{T}\boldsymbol{b})+\boldsymbol{b}^T\boldsymbol{B}^{-1}\boldsymbol{b} \\
&= \delta\boldsymbol{r}^T\boldsymbol{C}_{\rm white}^{-1}\delta\boldsymbol{r}-\hat{\boldsymbol{b}}^T\left(\boldsymbol{T}^T\boldsymbol{C}_{\rm white}^{-1}\boldsymbol{T}+\boldsymbol{B}^{-1}\right)\hat{\boldsymbol{b}}+\left(\boldsymbol{b}-\hat{\boldsymbol{b}}\right)^T\left(\boldsymbol{T}^T\boldsymbol{C}_{\rm white}^{-1}\boldsymbol{T}+\boldsymbol{B}^{-1}\right)\left(\boldsymbol{b}-\hat{\boldsymbol{b}}\right),
\end{aligned}
\tag{4.4.5}
$$

where

$$
\hat{\boldsymbol{b}} \equiv \left(\boldsymbol{T}^T\boldsymbol{C}_{\rm white}^{-1}\boldsymbol{T}+\boldsymbol{B}^{-1}\right)^{-1}\boldsymbol{T}^T\boldsymbol{C}_{\rm white}^{-1}\delta\boldsymbol{r}. \tag{4.4.6}
$$

As a result, only the last term depends on the parameters $\boldsymbol{b}$ and the Gaussian integration can be performed as

$$
\int_{-\infty}^{\infty}\exp\left(-\frac{1}{2}\left(\boldsymbol{b}-\hat{\boldsymbol{b}}\right)^T\left(\boldsymbol{T}^T\boldsymbol{C}_{\rm white}^{-1}\boldsymbol{T}+\boldsymbol{B}^{-1}\right)\left(\boldsymbol{b}-\hat{\boldsymbol{b}}\right)\right)d\boldsymbol{b} = \sqrt{\frac{(2\pi)^{N_{\rm TM}+2N_{\rm red}}}{\det\left(\boldsymbol{T}^T\boldsymbol{C}_{\rm white}^{-1}\boldsymbol{T}+\boldsymbol{B}^{-1}\right)}}. \tag{4.4.7}
$$

The marginalized posterior probability distribution therefore can be calculated as follows

$$
\begin{aligned}
&p(\boldsymbol{\phi},\boldsymbol{\eta}|\delta\boldsymbol{t},\mathcal{M}) \\
&= \int_{-\infty}^{\infty}p(\boldsymbol{\theta},\boldsymbol{\eta}|\delta\boldsymbol{t},\mathcal{M})d\boldsymbol{b} \\
&= \frac{1}{\sqrt{(2\pi)^{N_{\rm TOA}}\det(\boldsymbol{C}_{\rm white})\det(\boldsymbol{B})\det\left(\boldsymbol{T}^T\boldsymbol{C}_{\rm white}^{-1}\boldsymbol{T}+\boldsymbol{B}^{-1}\right)}} \\
&\times\exp\left(-\frac{1}{2}\left[\delta\boldsymbol{r}^T\boldsymbol{C}_{\rm white}^{-1}\delta\boldsymbol{r}-(\boldsymbol{T}^T\boldsymbol{C}_{\rm white}^{-1}\delta\boldsymbol{r})^T\left(\boldsymbol{T}^T\boldsymbol{C}_{\rm white}^{-1}\boldsymbol{T}+\boldsymbol{B}^{-1}\right)^{-1}\boldsymbol{T}^T\boldsymbol{C}_{\rm white}^{-1}\delta\boldsymbol{r}\right]\right) \\
&\times\frac{p(\boldsymbol{\eta}|\mathcal{M})p(\boldsymbol{\phi}|\mathcal{M})}{p(D|\mathcal{M})}.
\end{aligned}
\tag{4.4.8}
$$

TM noise was defined as a hierarchical model in the previous section, but there is no prior knowledge about parameters $\boldsymbol{\epsilon}$. In order to take this into account, it is further assumed that the values of the each hyperparameter Φ_l are much larger than the possible variances in the PTAs analysis. In this case, similar prior values are given over a range of possible values for each parameter, which means that there is no special value as prior information for each parameter[8)]. The prior probability distribution of the hyperparameter Φ_l are

$$p(\Phi_l|\mathcal{M}) = \delta(\Phi_l - m_l), \tag{4.4.9}$$

where m_l is a extremely large value. Then, the marginalization over the parameters Φ_l can be performed:

$$\begin{aligned}
&p(\boldsymbol{\phi}, A_{\rm red}, \gamma_{\rm red}|\delta\boldsymbol{t}, \mathcal{M}) \\
&= \int_{-\infty}^{\infty} p(\boldsymbol{\phi}, \boldsymbol{\eta}|\delta\boldsymbol{t}, \mathcal{M}) d\boldsymbol{\Phi} \\
&= \frac{1}{\sqrt{(2\pi)^{N_{\rm TOA}} \det(\boldsymbol{C}_{\rm white}) \det(\boldsymbol{B}) \det\left(\boldsymbol{T}^T \boldsymbol{C}_{\rm white}^{-1} \boldsymbol{T} + \boldsymbol{B}^{-1}\right)}} \\
&\times \exp\left(-\frac{1}{2}\left[\delta\boldsymbol{r}^T \boldsymbol{C}_{\rm white}^{-1} \delta\boldsymbol{r} - (\boldsymbol{T}^T \boldsymbol{C}_{\rm white}^{-1} \delta\boldsymbol{r})^T \left(\boldsymbol{T}^T \boldsymbol{C}_{\rm white}^{-1} \boldsymbol{T} + \boldsymbol{B}^{-1}\right)^{-1} \boldsymbol{T}^T \boldsymbol{C}_{\rm white}^{-1} \delta\boldsymbol{r}\right]\right) \\
&\times \frac{p(A_{\rm red}, \gamma_{\rm red}|\mathcal{M}) p(\boldsymbol{\phi}|\mathcal{M})}{p(D|\mathcal{M})},
\end{aligned} \tag{4.4.10}$$

where

$$\boldsymbol{B} = \mathrm{diag}(m_1, m_2, \cdots m_l, \Xi_1, \Xi_2, \cdots \Xi_k). \tag{4.4.11}$$

Note that, in the absence of knowledge of parameters, a uniform distribution is often used as a prior probability distribution. In order to perform the marginalization, it is reasonable to assume the uniform prior $p(\theta|\mathcal{M}) \propto 1$ in the range $\theta \in (-\infty, \infty)$. However, this distribution is not a probability distribution, because it cannot be normalized. Such a prior distribution is called improper prior distribution and special attention must be paid when we use it [61]. Since we did not want to use improper prior distribution, we used a normal distribution with very large variance for the TM parameters. This distribution is proper and can be regarded as an approximation of the uniform distribution. We set each hyperparameter value m_l to 10^{80}, which is sufficiently large for PTAs analysis.

As mentioned earlier, this marginalized posterior probability distribution is for a single pulsar. The marginalized posterior probability distribution using multiple pulsars can be obtained by multiplying the above equations of each pulsar except for the prior

[8)] As a matter of fact, we know that the equation $\boldsymbol{n}_{\rm TM} = \boldsymbol{M}\boldsymbol{\epsilon}$ is correct when $\boldsymbol{\epsilon}$ is small enough, and we can obtain uncertainties of the timing model parameters. Therefore, we might have to use the uncertainties as variances of the Gaussian prior distribution.

probability distribution of parameters common to all pulsars, and after that, multiplying the prior probability distribution of parameters common to all pulsars.

When actually calculating the posterior distribution, how to calculate a determinant and an inverse of a matrix is important to reduce computation time. Therefore we briefly describe the calculation. In the case of $\boldsymbol{C}_{\mathrm{white}}$, since $\boldsymbol{C}_{\mathrm{white}}$ is the block diagonal matrix, the determinant and the inverse can be calculated independently for each block. For each block, the matrix determinant lemma[9)] and the Sherman-Morrison formula[10)] can be used. In the case of $\boldsymbol{B}$, since $\boldsymbol{B}$ is the diagonal matrix, the determinant is the product of each element. In the case of $\boldsymbol{T}^T\boldsymbol{C}_{\mathrm{white}}^{-1}\boldsymbol{T}+\boldsymbol{B}^{-1}$, the Cholesky decomposition which expresses a matrix as a product of an upper triangular matrix and its transpose can be used to this matrix. Using the upper triangular matrix, the equation $(\boldsymbol{T}^T\boldsymbol{C}_{\mathrm{white}}^{-1}\boldsymbol{T}+\boldsymbol{B}^{-1})\boldsymbol{x}=\boldsymbol{T}^T\boldsymbol{C}_{\mathrm{white}}^{-1}\delta\boldsymbol{r}$ for $\boldsymbol{x}$ is solved rather than computing the inverse of $\boldsymbol{T}^T\boldsymbol{C}_{\mathrm{white}}^{-1}\boldsymbol{T}+\boldsymbol{B}^{-1}$ itself. The determinant can be calculated as twice the product of the diagonal elements of the upper triangular matrix.

4.5 Prior Probability Distribution

In this section, we describes the prior probability distribution. We use specific knowledge only for the mass errors of each planet as the prior information. Using the propagation of uncertainty law, the variances of δM^{J}, δM^{S}, and δM^{N} are calculated from the IAU 2009 system of astronomical constants, and the variance of δM^{U} is calculated from the values in the article [62] which is newer than the IAU 2009 system of astronomical constants. Then we assume a normal distribution for the mass errors of each planet and apply the obtained variances. For parameters without specific knowledge, we use a log-uniform distribution for parameters which are need to be searched over several orders of magnitude with only positive values, and we use a uniform distribution for the other parameters. The range of the log-uniform distribution and the uniform distribution is taken sufficiently wider than the value that the parameter would take. The parameters and their prior probability distribution used in this thesis are given in Table 4.1.

Regarding the amplitude of the FDM signal, we especially consider both cases of uniform distribution and log-uniform distribution as in the article [38]. The uniform distribution is used to give upper limits, and the log-uniform distribution is used for the model comparison, and the reason for this is as follows. If there is a FDM signal, for example by inserting it into data, the prior probability distribution is updated to a posterior probability distribution having a peak at the correct values of the parameters of the FDM. In this case, both prior probability distributions give similar posterior probability distributions. In practice, however, it is not known whether there is a FDM signal in the data, and even if the data is used, the posterior probability distribution may not be updated much from the prior probability distributions of the parameters of the FDM. In this practical case, the posterior probability distribution is affected by the shape

[9)] $\det(\boldsymbol{A}+\boldsymbol{u}\boldsymbol{v}^T)=(1+\boldsymbol{v}^T\boldsymbol{A}^{-1}\boldsymbol{u})\det(\boldsymbol{A})$

[10)] $(\boldsymbol{A}+\boldsymbol{u}\boldsymbol{v}^T)^{-1}=\boldsymbol{A}^{-1}-\dfrac{\boldsymbol{A}^{-1}\boldsymbol{u}\boldsymbol{v}^T\boldsymbol{A}^{-1}}{1+\boldsymbol{v}^T\boldsymbol{A}^{-1}\boldsymbol{u}}$

Table 4.1: Prior Probability Distribution

parameter	description	prior probability distribution
FDM signal		
Ψ	amplitude	Uniform[10^{-18}, 10^{-11}] (for upper limit)
		logUniform[-18, -11] (for model comparison)
f [Hz]	frequency	logUniform[$\log f - 0.015$, $\log f + 0.015$][11)]
α_e [rad]	phase at Earth	Uniform[0, 2π]
α_p [rad]	phase at pulsar	Uniform[0, 2π]
red noise		
$A_{\rm red}$	amplitude	logUniform[-20, -11]
γ	spectral index	Uniform[0.02, 6.98]
SSE noise		
$\delta M^{\rm J}$ [$M_\odot$]	mass error of Jupiter	$\mathcal{N}(0,\ 1.55 \times 10^{-11})$
$\delta M^{\rm S}$ [$M_\odot$]	mass error of Saturn	$\mathcal{N}(0,\ 8.17 \times 10^{-12})$
$\delta M^{\rm U}$ [$M_\odot$]	mass error of Uranus	$\mathcal{N}(0,\ 5.72 \times 10^{-11})$
$\delta M^{\rm N}$ [$M_\odot$]	mass error of Neptune	$\mathcal{N}(0,\ 7.96 \times 10^{-11})$
$\delta a^{\rm J}_\mu$	small offsets of parameters based on PCA bases	Uniform[-0.05, 0.05])
δz [rad/year]	rotation rate around ecliptic pole	Uniform[-10^{-9}, 10^{-9}]
white noise		
e_a	EFAC parameter	Uniform[0.001, 10] (for pre-analysis)
q_a [s]	EQUAD parameter	logUniform[-10, -4] (for pre-analysis)
j_a [s]	ECORR parameter	logUniform[-8.5, -4] (for pre-analysis)

of the prior probability distribution of the amplitude of the FDM signal. Considering the shape of the prior probability distribution, the log-uniform distribution allows smaller amplitude of the FDM signal than the uniform distribution, so that the upper limit obtained using Eq. (1.0.8) also decreases accordingly. Consequently, if one wants to give a conservative upper limit, the log-uniform distribution is not suitable. Furthermore, when we actually analyze the data used in this thesis, the posterior distribution obtained by using the log-uniform distribution is often have a value up to the lower limit given to the log-uniform distribution. This means that the upper limit depends on the lower limit of the log-uniform distribution, so that if the lower limit is decreased, the upper limit can be reduced. This is another reason why the logarithmic uniform distribution is not suitable for giving an upper limit. On the other hand, this property of a logarithmic uniform distribution is preferable for computing the Bayes factor (1.0.11), because the Bayes factor often gives a finite value with a fixed value $\Psi_0 = 10^{-18}$ which is a very small value as the lower limit of the prior probability distribution.

As is done in [52, 63, 38], we analyze the white noises in advance before the main analysis. The resulting MCMC chains are used to calculate the value that maximizes the one-dimensional posterior probability distribution corresponding to each white noise, where this value is called the maximum a posteriori (MAP) value. The main analysis is performed by fixing the possible values of the white noise parameter to the MAP value. See the section 4.7 for the pre-analysis.

4.6 Markov chain Monte Carlo simulation

The MCMC simulation can be used to generate samples from the posterior probability distribution. The MCMC method we used is called parallel tempering. In the parallel

tempering method, a concept of temperature is introduced, and the MCMC simulations of different temperatures are executed in parallel. The advantage of parallel tempering is that it is possible to reduce the tendency of the samples of the posterior distribution to be trapped in a local minimum, compared to the Metropolis-Hastings method which is the one of the most famous MCMC methods [60]. We carry out the analysis using four temperatures $T = 1.00, 4.64, 21.5, 100$.

In order to perform the parallel tempering, we use the software package PTMCMC-Sampler[12)] [64] via PAL2[13)] [65] which is a Bayesian inference package for PTA and can include the PTMCMCSampler. Regarding models not implemented in the PAL2, the FDM signal is implemented like the continuous gravitational waves and the SSE noise is implemented like any other noises. Following the article [52], we use adaptive Metropolis [66], single component adaptive Metropolis [67], and differential evolution [68], as a proposal algorithm which is used to generate next samples using past samples. Furthermore, we also use a simple proposal algorithm to generate the next sample of each parameter by proposal distribution which is the same distribution as the probability distribution. All of these proposal algorithms are used in a single MCMC simulation and which one is used is chosen randomly for each proposal in the MCMC simulation. In this thesis, we use the value written in the PAL2 for each variable used in PTMCMCSampler, unless specifically mentioned.

4.7 Pre-analysis

As is usual [52, 63, 38], in order to obtain the MAP values of the parameters of the white noise, we analyze the white noise first before the main analysis. By doing this, in the main analysis, the number of free parameters can be reduced, and the inverse matrix and determinant of the white noise mentioned in the section 4.4 only need to be calculated once at the beginning of MCMC simulation. In the pre-analysis, we performed independent analysis for each pulsar, and we used the model which contains the red noise in addition to white noise. We ran the MCMC simulation with 10^6 iterations and removed the first 25% as a burn-in period, where the burn-in period is the period during which samples have not yet been obtained from the target distribution.

Table 4.2 shows the results of the white noise and the red noise obtained by the pre-analysis. The obtained posterior distribution is expressed by the MAP value and the 95% confidence interval. At the Green Bank Observatory, the receivers are Rcvr_800 and Rcvr1_2, and the backend system is GASP in early observations and GUPPI in later observations. Similarly, at the Arecibo Observatory, the receivers are L-wide and S-wide, and the backend system is ASP in early observations and PUPPI in later observations. Please see the article [32] for details on the receiver and the backend system.

The reason for including the red noise in the model is that the red noise is the stochastic noise same as the white noise and it can become white noise when the spectral index becomes zero. However, if the one-dimensional posterior probability distribution

[12)] https://github.com/jellis18/PTMCMCSampler
[13)] https://github.com/jellis18/PAL2

Table 4.2: Result of pre-analysis

parameter	J0613-0200	J1012+5307	J1600-3053	J1713+0747	J1744-1134	J1909-3744
EFAC noise						
Rcvr_800_GASP	$1.096^{+0.059}_{-0.059}$	$1.138^{+0.049}_{-0.042}$	$1.19^{+0.11}_{-0.11}$	$1.134^{+0.050}_{-0.054}$	$1.168^{+0.073}_{-0.064}$	$0.984^{+0.081}_{-0.060}$
Rcvr_800_GUPPI	$1.164^{+0.041}_{-0.032}$	$1.182^{+0.023}_{-0.023}$	$1.117^{+0.025}_{-0.040}$	$1.066^{+0.023}_{-0.020}$	$1.070^{+0.027}_{-0.024}$	$1.041^{+0.023}_{-0.019}$
Rcvr1_2_GASP	$1.061^{+0.056}_{-0.053}$	$1.054^{+0.044}_{-0.041}$	$1.155^{+0.096}_{-0.148}$	$1.087^{+0.056}_{-0.060}$	$0.991^{+0.080}_{-0.065}$	$0.977^{+0.054}_{-0.060}$
Rcvr1_2_GUPPI	$1.080^{+0.023}_{-0.023}$	$1.081^{+0.021}_{-0.018}$	$1.062^{+0.018}_{-0.019}$	$1.040^{+0.015}_{-0.014}$	$1.079^{+0.028}_{-0.026}$	$1.049^{+0.017}_{-0.013}$
L-wide_ASP				$1.013^{+0.062}_{-0.048}$		
L-wide_PUPPI				$1.091^{+0.026}_{-0.021}$		
S-wide_ASP				$1.114^{+0.066}_{-0.058}$		
S-wide_PUPPI				$1.110^{+0.038}_{-0.034}$		
EQUAD noise[14)]						
Rcvr_800_GASP	$-8.5^{+1.7}_{-1.5}$	$-6.68^{+0.18}_{-3.22}$	$-7.7^{+1.5}_{-2.2}$	$-6.97^{+0.18}_{-2.93}$	$-6.469^{+0.079}_{-0.085}$	$-6.620^{+0.046}_{-0.056}$
Rcvr_800_GUPPI	$-6.677^{+0.099}_{-0.188}$	$-6.348^{+0.062}_{-0.059}$	$-6.45^{+0.14}_{-3.45}$	$-7.14^{+0.14}_{-2.75}$	$-6.598^{+0.036}_{-0.045}$	$-7.344^{+0.090}_{-0.119}$
Rcvr1_2_GASP	$-9.74^{+3.16}_{-0.17}$	$-6.51^{+0.19}_{-3.38}$	$-6.34^{+0.17}_{-3.54}$	$-7.29^{+0.16}_{-2.59}$	$-6.382^{+0.072}_{-0.097}$	$-7.40^{+0.18}_{-2.41}$
Rcvr1_2_GUPPI	$-9.65^{+2.75}_{-0.27}$	$-6.50^{+0.11}_{-0.25}$	$-8.3^{+1.2}_{-1.7}$	$-8.01^{+0.24}_{-1.93}$	$-6.681^{+0.041}_{-0.051}$	$-8.04^{+0.19}_{-1.88}$
L-wide_ASP				$-7.54^{+0.11}_{-0.23}$		
L-wide_PUPPI				$-7.89^{+0.13}_{-1.78}$		
S-wide_ASP				$-8.46^{+0.93}_{-1.48}$		
S-wide_PUPPI				$-7.64^{+0.16}_{-2.24}$		
ECORR noise[a]						
Rcvr_800_GASP	$-7.50^{+0.69}_{-0.96}$	$-8.08^{+1.37}_{-0.38}$	$-8.472^{+2.269}_{+0.019}$	$-7.45^{+0.49}_{-1.02}$	$-6.63^{+0.25}_{-1.38}$	$-7.95^{+0.76}_{-0.52}$
Rcvr_800_GUPPI	$-6.74^{+0.26}_{-0.32}$	$-8.480^{+1.517}_{0.010}$	$-6.20^{+0.13}_{-0.24}$	$-6.609^{+0.092}_{-0.142}$	$-6.40^{+0.12}_{-0.17}$	$-7.19^{+0.16}_{-0.24}$
Rcvr1_2_GASP	$-7.94^{+1.43}_{-0.51}$	$-6.59^{+0.28}_{-1.83}$	$-6.74^{+0.31}_{-1.70}$	$-7.11^{+0.25}_{-0.54}$	$-6.16^{+0.14}_{-0.20}$	$-8.31^{+0.89}_{-0.17}$
Rcvr1_2_GUPPI	$-6.77^{+0.15}_{-1.64}$	$-6.55^{+0.15}_{-1.45}$	$-6.81^{+0.16}_{-0.34}$	$-7.115^{+0.067}_{-0.091}$	$-6.372^{+0.090}_{-0.087}$	$-7.113^{+0.066}_{-0.079}$
L-wide_ASP				$-6.97^{+0.14}_{-0.11}$		
L-wide_PUPPI				$-7.061^{+0.087}_{-0.069}$		
S-wide_ASP				$-6.95^{+0.14}_{-0.18}$		
S-wide_PUPPI				$-7.03^{+0.11}_{-0.10}$		
red noise						
$A_{\rm red}$[a]	$-13.15^{+0.17}_{-0.68}$	$-12.67^{+0.14}_{-0.16}$	$-13.45^{+0.16}_{-6.36}$	$-14.46^{+0.39}_{-3.74}$	$-13.44^{+0.33}_{-3.75}$	$-14.13^{+0.35}_{-1.96}$
γ	$1.26^{+2.08}_{-0.99}$	$0.96^{+0.79}_{-0.61}$	$0.17^{+6.49}_{-0.10}$	$2.3^{+3.9}_{-1.6}$	$2.9^{+3.9}_{-1.6}$	$6.899^{-0.021}_{-5.295}$

of the parameter of the white noise has a sharp peak, it was confirmed that the MAP value of the parameter does not change very much regardless of the presence or absence of the red noise model. In particular, it is know that the red noise of the PSR 1909-3744 can take wide parameter values [35], but the above result was obtained. Therefore, this result suggests that the white noise can be analyzed in advance.

Chapter 5

Result

In this section we describe the upper limits on the amplitude of the FDM signal Eq. (4.2.1) and how much the FDM signal is absorbed by other noises. All our result was calculated using six pulsars: PSRs J0613-0200, J1012+5307, J1600-3053, J1713+0747, J1744-1134, and J1909-3744 in the NANOGrav 11-year data set.

5.1 Upper limits

We calculated the 95% confidence upper limits on the amplitude of the FDM signal Eq. (4.2.1) by the Bayesian analysis. We ran all the MCMC simulation with 10^6 iterations and removed the first 25% as a burn-in period. As the prior probability distribution of the amplitude of the FDM signal we considerd two cases: the uniform prior and the log-uniform prior. The uniform prior was used to place the conservative upper limits, the log-uniform prior was used to calculate the Bayes factors, where the upper limits were caluculated using the Eq. (1.0.8) and the Bayes factors were calculated using Eq. (1.0.11). In order to see the effect of including the SSE noise in the model on the results, we also calculated the upper limits and the Bayes factors when the SSE noise is not included in the model. See Appendix B for how accurately the FDM can be detected by our Bayesian analysis.

In Figure 5.1, we show the upper limits and the Bayes factors of the amplitude Ψ as a function of the frequency f and the FDM mass m. The relation between the frequency f and the FDM mass m is given by Eq. (4.2.4). First, in the above plot, the black solid and dashed lines denote the upper limit using uniform prior and log-uniform prior, respectively. Here, we plotted the results obtained using log-uniform prior, but as we mentioned in the section 4.5, we regard the results obtained by the uniform prior as conservative upper limits. The red solid and dashed lines denote the upper limit obtained when the SSE noise was not included in the model, and using uniform-prior and log-uniform prior, respectively. The bold black line denotes the upper limit of the Bayesian analysis obtained in [11]. The green line denotes the predicted amplitude of the FDM signal given by Eq. (4.2.3) with $\rho = 0.4\mathrm{Gev/cm}^3$. Note that it does not mean that there is the FDM signal on all of this line, it is observed at one point on this line,

depending on the mass of the FDM. The purple vertical lines denote the inverse of the observation times of pulsars and corresponds to PSRs J1744-1134, J1012+5307, J1909-3744, J1713+0747, J0613-0200, and J1600-3053 in order from the left. We regard the purple vertical line on the leftmost side as the lower limit of the frequency at which the PTA is sensitive to the signal of FDM. One simple reason why the inverse of the observation time is lower limit of the frequency that it would be difficult to detect a signal with a longer wavelength than the observation time. A slightly more specific reason is that some of the signal at lowest frequency is removed by fitting the pulsar spin periods when creating the residuals [36, 37]. Furthermore, in the model used in this thesis, the TM noise is included to take into account the uncertainty of the fitting. The TM noise corresponding to pulsar spin periods induces uncertainty in the analysis of the FDM signal at the lowest frequency, because we marginalized the posterior probability distribution using the uninformative prior for the parameters $\boldsymbol{\epsilon}$. Next, in the bottom plot, the black and red dots denote the mean value of the Bayes factor using the model with and without the SSE noise, respectively. The unbiased standard deviation is used for error bars. Only to make the plot easier to see, when the Bayes factor exceeds 20, it is represented by the upper triangle and the mean value and the unbiased standard deviations of the Bayes factor is written above it.

First we consider the red results obtained when the SSE noise is not included in the model. It turns out that the upper limits for the log-uniform distribution gives stronger limits than for the uniform distribution, but the difference is small. The reason the difference is small is that the Bayes factor exceeds 3 when the frequency becomes $10^{-8.19}$ Hz (1.34×10^{-23} eV) or lower. According to the Table A.1, the Bayes factor exceeds 3 means that there is a signal that is somewhat similar to the FDM signal. Therefore, whichever prior probability distribution is used, the value of the posterior probability distribution tends to be large at the parameter values of that signal, and as a result the upper limits does not change so much. Also, in cases where the frequencies are $10^{-8.52}$ and $10^{-8.46}$Hz (6.24×10^{-23} and 7.17×10^{-23} eV), the Bayes factor exceeds 20. Thus, at these frequencies, the presence of the FDM signal is strongly supported, but it should be noted that the fitting of the pulsar spin periods biases the analysis results. From the above, it was found that the FDM signal is positively supported in the wide frequency range. However, from a physical point of view, it is hard to think that FDM signals has been found, because the upper limit obtained is about an order of magnitude greater than the expected amplitude and also FDM signals would have only a certain frequency.

Next, we consider the black result obtained when the SSE noise is included in the model. This result is our main result. Compared with the case where SSE noise is included in the model, it can be seen that the upper limits of the amplitude of the FDM signal obtained using uniform distribution does not change much. However, the difference between the upper limits obtained from the different prior probability distributions is large. The reason for this is that all Bayes factors are smaller than 3 and in most cases they do not exceed 1, for the opposite reason to that mentioned in the previous paragraph. The Bayes factor is less than 1 means that the probability that

the model without the signal of the FDM $p(\mathcal{M}_2|d)$ is superior to the model with it $p(\mathcal{M}_1|d)$. Therefore, in this case we conclude that no FDM signal has been detected. At frequencies $10^{-8.46}$Hz (7.17×10^{-24} eV) or lower, the Bayes factor is larger than 1, but it is too early to mention the existence of the FDM signal, because it is close to the lower limit of the frequency. The red and black results show that the Bayes factor is smaller when the SSE noise is considered. Thus, we conclude that the SSE noise can mimic the FDM signal. This result would be inferred from the result that the SSE noise can mimic the stochastic gravitational wave background [38]. In comparison with the published Bayesian upper limits of the amplitude of the FDM signal using the PPTA 12-year data set [11], i.e. comparing the black and the bold black lines, we found that stronger upper limits were obtained when the frequency was in the range from $10^{-8.34}$ to $10^{-8.19}$Hz (from 9.45×10^{-24} to 1.34×10^{-23} eV). In this range, up to three times stronger upper limits were obtained, and in other region, about the same upper limits were obtained.

It is also important to see the upper limit on the energy density of the dark matter near the Earth rather than the amplitude of the FDM signal. Thus, we convert the amplitude of the FDM signal into the energy density using Eq. (4.2.3), and the result is plotted in Figure 5.2. Note that the bold black line denotes the upper limit on the energy density with the Bayesian analysis in [11] (taken from Figure 4). As we can see from Figure 5.2, our main upper limit represented by the black line is 7 or less in the range from $10^{-8.55}$ to $10^{-8.01}$ Hz (from 5.83×10^{-24} to 2.02×10^{-23} eV) where we analyzed. The strongest upper limit on the the energy density is $2\,\mathrm{GeV/cm^3}$ at the frequency $10^{-8.28}$ Hz (1.09×10^{-23} eV).

5.2 Fixed noise analysis

We analyzed the red noise and the SSE noise first and calculated the upper limits of the amplitude of the FDM signal Eq. (4.2.1) using the obtained MAP values of the parameters. We ran the MCMC simulation with 10^6 iterations for analysis of red noise and SSE noise and with 10^5 iterations for analysis of the FDM signal, and in both cases we removed the first 25% as a burn-in period. The result of the red noise and the SSE noise used for the fixed noise analysis are summarized in Table 5.1. The obtained posterior distribution is expressed by the MAP value and the 95% confidence interval.

As in the previous section, we calculated two cases of uniform and log-unifrom distributions as the prior probability distribution of the amplitude of the FDM signal. The results are plotted in Figure 5.3 which is the similar plot as Figure 5.1. The solid and dashed lines indicate that the unifrom and the loguniform prior were used, respectively.

The reason for doing this analysis is to know how much the red noise and the SSE noise can absorb the signal of the FDM. Note that this analysis is not intended to give the upper limits on the amplitude of the FDM signal. The FDM signal, the red noise and the noise induced by Jupiter in the SSE noise have similar waveforms and any of these can not be analyzed in advance. The reason is as follows. The red noise is a random process, but it is known that it mimics a periodic waveform with a lowest frequency in

Table 5.1: Red noise and SSE noise used for fixed noise analysis

parameter	J0613-0200	J1012+5307	J1600-3053	J1713+0747	J1744-1134	J1909-3744
red noise						
A_{red} [1)]	$-13.20^{+0.20}_{-0.73}$	$-12.68^{+0.14}_{-0.16}$	$-13.51^{+0.10}_{-6.34}$	$-19.939^{+5.436}_{0.055}$	$-13.51^{+0.33}_{-2.31}$	$-14.05^{+0.17}_{-5.77}$
γ	$1.36^{+2.33}_{-0.98}$	$1.07^{+0.74}_{-0.63}$	$0.0897^{+6.6316}_{-0.0069}$	$1.8^{+4.9}_{-1.6}$	$2.8^{+4.0}_{-1.2}$	$0.74^{+5.97}_{-0.62}$
common to all pulsars						
SSE noise						
δM^{J}	$-2 \times 10^{-12^{+3.3\times10^{-11}}_{-3.0\times10^{-11}}}$					
δM^{S}	$1 \times 10^{-12^{+1.6\times10^{-11}}_{-1.6\times10^{-11}}}$					
δM^{U}	$1 \times 10^{-11^{+1.0\times10^{-10}}_{-1.2\times10^{-10}}}$					
δM^{N}	$1 \times 10^{-11^{+1.5\times10^{-10}}_{-1.7\times10^{-10}}}$					
δa_1^{J}	$-0.0046^{+0.0109}_{-0.0099}$					
δa_2^{J}	$0.004^{+0.019}_{-0.018}$					
δa_3^{J}	$-0.0128^{+0.0071}_{-0.0083}$					
δa_4^{J}	$-0.0123^{+0.0117}_{-0.0077}$					
δa_5^{J}	$0.0044^{+0.0080}_{-0.0087}$					
δa_6^{J}	$0.008^{+0.012}_{-0.019}$					
δz	$-2.0 \times 10^{-10^{+1.15\times10^{-09}}_{-7.4\times10^{-10}}}$					

the case of the steep power law, for example, please see [69] and references therein. The noise induced by the mass error of Jupiter has the frequency which corresponding to the inverse of the orbital period, and the noises induced by each error of orbital elements of Jupiter also have its frequency or twice of its frequency. Since Jupiter's orbital period is 11.86 yr, Jupiter causes noises with frequencies close to the lowest frequency in the 11-year dataset we used. From the above, we consider that this analysis is not suitable for giving an upper limit to the amplitude of the FDM signal, and the obtained results are not regarded as the upper limits of the amplitude of the FDM signal.

It can be seen from Figure 5.3 that the values of the upper limits are drastically smaller than the result obtained in the previous section. In particular, when using the log-uniform prior, surprisingly, the upper limits are smaller than the predicted amplitude in some range. As for Bayesian factors, they are all smaller than 1, which is consistent with the fact that the upper limits are strongly influenced by the prior probability distribution. From this result, it is inferred that the FDM signal is well absorbed by the red noise and the SSE noise.

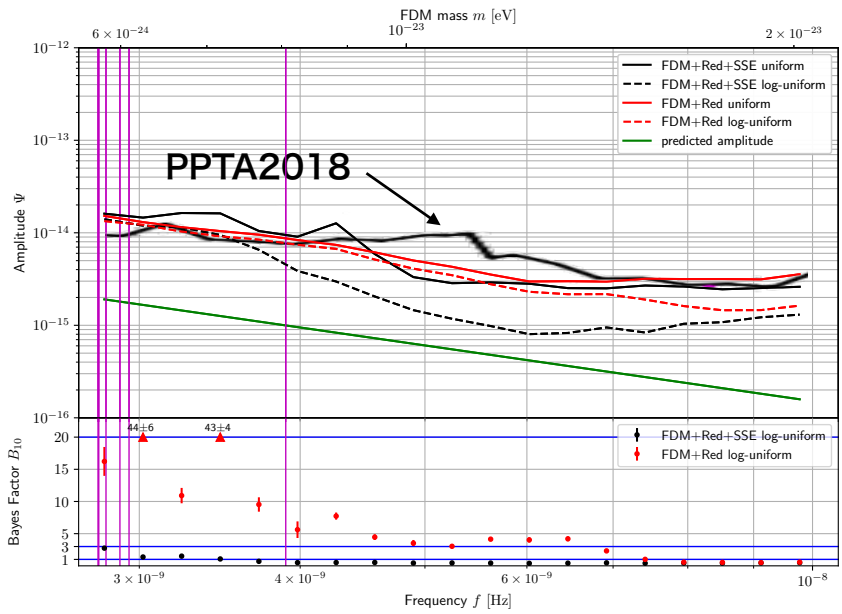

Figure 5.1: Top: The 95% upper limits on the amplitude of the FDM signal Ψ using the NANOGrav 11-year data set. As a prior probability distribution of the amplitude of the FDM signal, the uniform prior was used for the black solid lines and the log-uniform prior was used for black dashed lines. The red lines are the upper limit obtained when the SSE noise is not included in the model describing the observed data, and the solid and dashed lines indicate that unifrom and loguniform were used, respectively. The bold black line is the upper limit obtained by the Bayesian analysis of the PPTA data (taken from Figure 3 in [11]). The green line is the predicted amplitude of the FDM signal. The purple vertical line is the inverse of the observation time of the pulsars. Bottom: The values of the Bayes factor obtained when using log-uniform prior. The black and red indicate when the SSE noise is included in the model or not, respectively. To improve the visibility of the plot, when the value of the Bayes factor exceeds 20, the upper triangle is used.

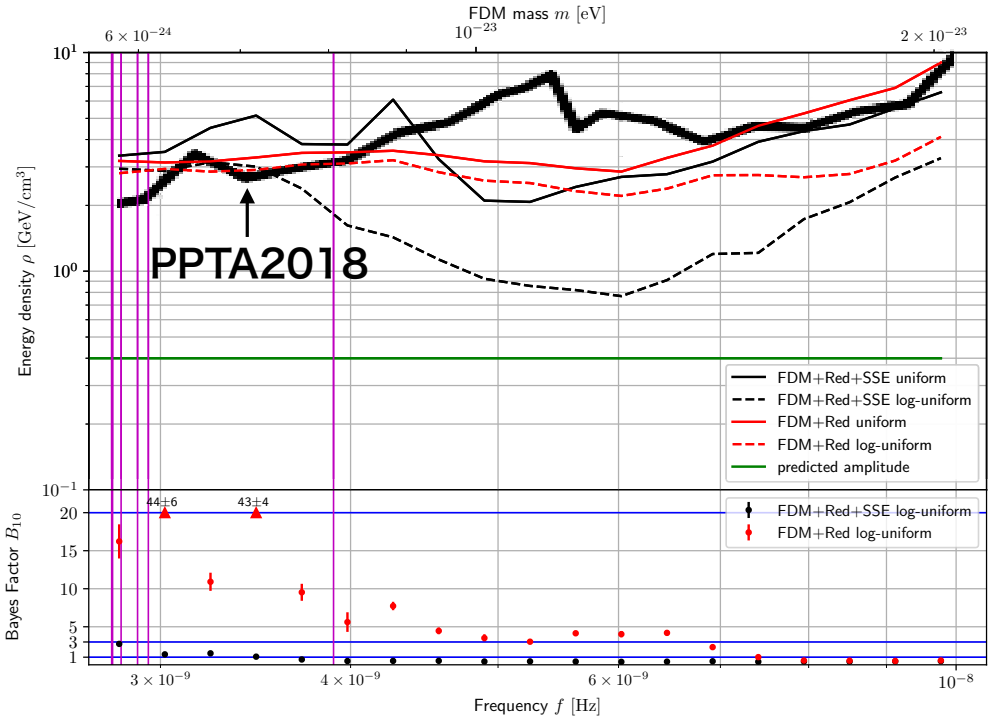

Figure 5.2: Top: The 95% upper limits on the energy density of the FDM ρ using the NANOGrav 11-year data set. This plot is the same as in Figure 5.1 except that the amplitude is converted to energy density. The bold black line denotes the upper limit obtained by the Bayesian analysis of the PPTA data (taken from Figure 4 in [11]). Bottom: The values of the Bayes factor obtained when using log-uniform prior. This plot is the same as in Figure 5.1.

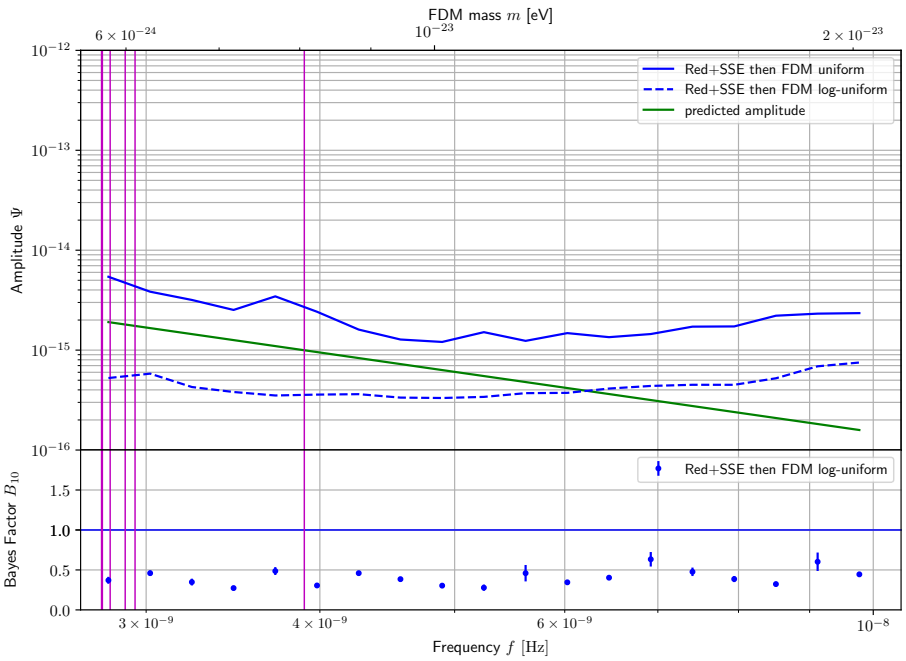

Figure 5.3: Similar plot to Figure 5.1. The FDM signal, the red noise and the noise induced by Jupiter in the SSE noise have similar waveforms and any of these can not be analyzed in advance. Therefore we do not regard this plot from such an analysis as the upper limits of the amplitude of the FDM signal. The purpose of this plot is to know how much the red noise and the SSE noise can absorb the signal of the FDM.

Chapter 6

Conclusion

We searched for the FDM signal Eq. (4.2.1) by performing the Bayesian analysis in the time domain using the NANOGrav 11-year Data Set. In Section 5.1, we gave the 95% confidence upper limit on the amplitude of the FDM signal. we found that probability that the FDM should be included in the model was less than 75% in all frequency region. Compared with the published Bayesian upper limit of the FDM using the PPTA 12-year data set [11], we found that our upper limit was up to 3 times stronger than the previous study when the frequency was in the range from $10^{-8.34}$ to $10^{-8.19}$Hz (9.45×10^{-24} to 1.34×10^{-23} eV in terms of the FDM mass). In other region, we also obtained the similar upper limit on the amplitude of the FDM signal. Since the amplitude of FDM can be converted to the energy density of the dark matter near the Earth, it is easy to obtain the upper limit of the energy density. The upper limit on the energy density was lower than $7\,\mathrm{GeV/cm^3}$ in the range from $10^{-8.55}$ to $10^{-8.01}$ Hz (from 5.83×10^{-24} to 2.02×10^{-23} eV) where we analyze. In particular, at a frequency of $10^{-8.28}$ Hz (a mass of 1.09×10^{-23} eV), we obtained the strongest upper limit $2\,\mathrm{GeV/cm^3}$. In addition to the main analysis, we also investigated the case where the SSE noise was not included in the model. In this case, we showed that we can not exclude the existence of the FDM, because the probability that the FDM should be included in the model was more than 75% in the frequency region $10^{-8.19}$ Hz or less. This results show that the Bayes factor is smaller when the SSE noise is considered. Thus, we conclude that the SSE noise can mimic the FDM signal, which would be inferred from the result that the SSE noise can mimic the stochastic gravitational wave background [38].

In Section 5.2, by analyzing the noise in advance, we examined how much the signal of the FDM was absorbed. In this case, we clarified that the probability that the FDM should be included in the model was much lower than 50% in all frequency region. Compared to our main analysis, we found that the upper limit on the amplitude of the FDM signal became very small. Note that it is inappropriate to analyze only the noise in advance, and we do not consider this to be an actual upper limit for the FDM. From this, it is expected that the signal of the FDM will be absorbed very well by analyzing the noise in advance.

Acknowledgements

I would like to thank my supervisor Prof. Soda of Institute of Cosmophysics Kobe University for useful discussions and collaborations. I am grateful to Prof. Kurashige of High Energy Group Department of Physics Kobe University for wide-ranging discussion. I would like to thank Assistant Prof. Noumi of Institute of Cosmophysics Kobe University for useful suggestions. I also would like to thank the members of Institute of Cosmophysics Kobe University. R.K. was supported by Grant-in-Aid for JSPS Research Fellow and JSPS KAKENHI Grant Numbers 17J00496.

Appendix A

Bayesian Parameter Estimation and Model Comparison

We review the Bayesian parameter estimation and the model comparison in the following paragraphs. For further details about the Bayesian data analysis, see for example [60, 70, 61].

The purpose of the Bayesian parameter estimation is to estimate the posterior probability distribution $p(\theta|D)$ of the parameters θ given the data D. Having the observed data, we can update our belief about the parameters using Bayes' rule, namely

$$p(\theta|D) = \frac{p(D|\theta)p(\theta)}{p(D)}. \tag{1.0.1}$$

In the above expression, the posterior probability distribution is interpreted as the strength of belief in the parameters based on the data, and $p(\theta)$ is the prior probability distribution, which is interpreted as the strength of belief in the parameters without the data. Then $p(D|\theta)$ is the likelihood function, which is the probability of the data given the parameters. Lastly, $p(D)$ is the evidence, which is the probability of the data. Using the law of total probability, the evidence is given by

$$p(D) = \int_\Omega d\theta\, p(D|\theta)p(\theta), \tag{1.0.2}$$

where Ω denotes the parameter space. For the purpose of the parameter estimation, the evidence can be regarded as a normalization constant, because it does not involve the parameter. It is reasonable to explicitly include in Eq. (1.0.1) the model $\mathcal{M}$ which assigns a meaning to the parameters. Given a model, we can rewrite Eq. (1.0.1):

$$p(\theta|D, \mathcal{M}) = \frac{p(D|\theta, \mathcal{M})p(\theta|\mathcal{M})}{p(D|\mathcal{M})}, \tag{1.0.3}$$

where

$$p(D|\mathcal{M}) = \int_\Omega d\theta\, p(D|\theta, \mathcal{M})p(\theta|\mathcal{M}). \tag{1.0.4}$$

More generally, considering a hierarchical model in which the parameters depend on the parameters, the prior probability distribution becomes $p(\theta, \eta|\mathcal{M})$, where η is called as a hyperparameter which is the parameter of the parameter θ. Applying the product rule for the conditional probability, the prior probability distribution can be written as

$$p(\theta, \eta|\mathcal{M}) = p(\theta|\eta, \mathcal{M})p(\eta|\mathcal{M}). \tag{1.0.5}$$

Then, using Bayes' rule Eq. (1.0.3), the posterior probability distribution would be written as

$$\begin{aligned} p(\theta, \eta|D, \mathcal{M}) &= \frac{p(D|\theta, \eta, \mathcal{M})p(\theta, \eta|\mathcal{M})}{p(D|\mathcal{M})} \\ &= \frac{p(D|\theta, \mathcal{M})p(\theta, \eta|\mathcal{M})}{p(D|\mathcal{M})}. \end{aligned} \tag{1.0.6}$$

The above equation tells us that the hyperparameter only affects the posterior probability distribution through parameters, that is, the likelihood function does not depend on the hyperparameter.

Although the model used in this study contains many parameters and hyperparameters, we are interested in only the amplitude of the FDM signal. Therefore, the posterior probability distribution is integrated over the parameters and the hyperparameters except for the amplitude of the FDM signal:

$$p(A|D, \mathcal{M}) = \int_{\Omega'} p(A, \boldsymbol{\theta}', \boldsymbol{\eta}|D, \mathcal{M}) d\boldsymbol{\theta}' d\boldsymbol{\eta}, \tag{1.0.7}$$

where $\boldsymbol{\theta}'$ is the vector which denotes the parameters except for the amplitude of the FDM signal, $\boldsymbol{\eta}$ is the vector which denotes the hyperparameters, and Ω' denotes the parameter space for $\boldsymbol{\theta}'$ and $\boldsymbol{\eta}$. This procedure is called marginalization. Using the posterior probability distribution for the amplitude of the FDM signal, we define the upper limit R by

$$\int_0^R p(A|D, \mathcal{M}) dA = 0.95. \tag{1.0.8}$$

The above equation means that the probability that the amplitude of the FDM signal is less than or equal to R is 95%. The purpose of parameter estimation in this thesis is to obtain this upper limit R.

It is not practical to calculate the posterior probability distribution for a lot of parameters, because the multiple integration of the denominator is generally difficult. Even if one can calculate the posterior distribution, one must calculate an integral like Eq. (1.0.7) to discuss the probability of a specific parameter. One way to avoid these problems is to use Markov Chain Monte Carlo (MCMC) method to generate samples from the posterior probability distribution instead of calculating the posterior probability distribution itself. Since the unnormalized posterior probability distribution is used in MCMC, we do not need to calculate the normalization constant, that is, the evidence.

Table A.1: Interpretation of the Bayes factor and the probability $p(\mathcal{M}_1|d)$

B_{12}	$p(\mathcal{M}_1\|d)$	Evidence in favor of $\mathcal{M}_1$ against $\mathcal{M}_2$
1-3	0.500-0.750	Not worth more than a bare mention
3-20	0.750-0.952	Positive
20-150	0.952-0.993	Strong
>150	>0.993	Very strong

In order to discuss a specific parameter after using the MCMC method, we simply select the samples of the parameter from the derived samples.

Analogous to the parameter estimation, we can also update our belief about the the model through the data with the Bayes' rule:

$$p(\mathcal{M}|D) = \frac{p(D|\mathcal{M})p(\mathcal{M})}{p(D)}. \tag{1.0.9}$$

If we have two competing models $\mathcal{M}_1$ and $\mathcal{M}_2$, for the Bayesian model comparison, it is often considered the ratio of Eq. (1.0.4) of two models. The ratio

$$\begin{aligned} \frac{p(\mathcal{M}_1|D)}{p(\mathcal{M}_2|D)} &= \frac{p(\mathcal{M}_1)}{p(\mathcal{M}_2)}\frac{p(D|\mathcal{M}_1)}{p(D|\mathcal{M}_2)}, \\ &\equiv \frac{p(\mathcal{M}_1)}{p(\mathcal{M}_2)}B_{12}, \end{aligned} \tag{1.0.10}$$

is called the odds ratio and the first ratio on the right-hand side is the prior odds ratio and the second ratio is the Bayes factor. The purpose of the model comparison procedures is to calculate the Bayes factor according to Eq. (1.0.4), and therefore the evidence becomes critically important unlike in the case of the parameter estimation. However, as described in the following paragraph, if two models compared are nested models, it is not necessary to calculate Eq. (1.0.4). The Table A.1 gives the interpretation of the Bayes factor in terms of the strength of the evidence. The second column of the Table A.1 refers to the probability $p(\mathcal{M}_1|D)$ under the assumption that the prior odds ratio is equal to unity: $p(\mathcal{M}_1) = p(\mathcal{M}_2) = 0.5$ [71, 72, 73]. In this thesis, since we have no prior knowledge of models, we set the prior odds ratio to 1. Therefore we can use the probability of the second column in the Table A.1.

For the nested models where two models contain the common parameters and one model has at least one additional parameter [74], calculation of the Bayes factor is significantly simplified. We compare the model $\mathcal{M}_1$ in which the parameters include the amplitude of the FDM signal and the model $\mathcal{M}_2$ in which the amplitude of the FDM signal is a fixed value Ψ_0 and the other parameters are same as those in the model $\mathcal{M}_1$. In the case of nested models, we can use the Savege-Dickey density ratio to calculate the Bayes factor [74, 75, 76, 72], namely,

$$B_{12} = \frac{p(\Psi = \Psi_0|\mathcal{M}_1)}{p(\Psi = \Psi_0|D, \mathcal{M}_1)}, \tag{1.0.11}$$

where we assumed the statistical independence between the amplitude of the FDM signal and the other parameters given the model $\mathcal{M}_1$ and assumed that the prior probability distribution of the parameters are the same for both models except for the amplitude of the FDM signal, that is,

$$p(\Psi, \theta'|\mathcal{M}_1) = p(\Psi|\mathcal{M}_1)p(\theta'|\mathcal{M}_2). \tag{1.0.12}$$

From the equation Eq. (1.0.11), it can be seen that this Bayes factor requires only the prior and the posterior probability distribution for Ψ at Ψ_0 under the model $\mathcal{M}_1$ instead of the evidences of each model. Since the prior probability distribution is given before the parameter estimation and the samples of the posterior probability distribution are obtained from the result of the parameter estimation, it is possible to calculate this Bayes factor immediately after the parameter estimation. Specifically, we calculate Eq. (1.0.11) for multiple small bins around the fixed value Ψ_0, then the average is used as the Bayes factor, and the unbiased standard deviation is used as the error bar. In this thesis, we use the lower limit in the log-uniform distribution for the amplitude of the FDM signal as the fixed value Ψ_0. Since this lower limit is sufficiently small, the model $\mathcal{M}_2$ can be regarded as a model with no FDM signal.

Appendix B

Simulated Signal

In order to investigate whether the signal can actually be detected by the MCMC simulation, we test the MCMC simulation using data composed of virtual signals. We made the following two data:

$$\text{Data1}: \quad \delta \boldsymbol{t} = \boldsymbol{s} + \boldsymbol{n}_{\text{red}} + \boldsymbol{n}_{\text{SSE}} + \boldsymbol{n}_{\text{equad}}, \quad f = 10^{-8.0}, \tag{2.0.1}$$

$$\text{Data2}: \quad \delta \boldsymbol{t} = \boldsymbol{s} + \boldsymbol{n}_{\text{red}} + \boldsymbol{n}_{\text{SSE}} + \boldsymbol{n}_{\text{equad}}, \quad f = 10^{-8.55}, \tag{2.0.2}$$

where the Data1 has the FDM frequency of $10^{-8.0}$ Hz, and the Data2 has the FDM frequency of $10^{-8.55}$ Hz. The frequencies $10^{-8.0}$ and $10^{-8.55}$ Hz are respectively the highest and lowest frequencies of the upper limit of the amplitude of the FDM signal calculated by us. It is considered that $10^{-8.0}$ Hz is easy to distinguish from other noises, while $10^{-8.55}$ Hz is not. We do not specifically mention the parameter values we used, but the RMS value is 10^{-4} s for the FDM signal, the red noise and the SSE noise, and 10^{-6} s for the equad.

The model we used is

$$\text{Model}: \quad \delta \boldsymbol{t} = \boldsymbol{s} + \boldsymbol{n}_{\text{TM}} + \boldsymbol{n}_{\text{red}} + \boldsymbol{n}_{\text{SSE}} + \boldsymbol{n}_{\text{equad}}. \tag{2.0.3}$$

As in Section 4.4, the posterior probability distribution is marginalized over the parameters of the red noise and TM noise. The timing fit has not been performed on the data, but the TM noise is added to investigate the decrease in sensitivity due to the design matrix. The values of the prior probability distribution in Section 4.5 are rewritten so that the prior probability distribution contains the value of simulated data parameters. The prior probability distribution of the amplitude of the FDM signal is log-uniform distribution. The prior probability distribution of the equad noise is fixed to the MAP value obtained by the pre-analysis, where both the data and the model of the pre-analysis include only the equad noise. The MCMC simulation is perfomed with 10^6 iterations and removed the first 25% as a burn-in period.

In order to confirm that our implementation is done correctly, we also examine the case where the TM noise is not included in the model except for a constant part with respect to the time of the TM noise. The reason for leaving only a constant part with

respect to the time of TM noise is to ignore the effect of subtracting the average when creating the data. Since it turned out that the posterior probability distribution did not converge when the iteration was 10^6, we fix the red noise and the SSE noise to the MAP value. For the MAP values, the red noise and the SSE noise are analyzed independently by creating noise data corresponding to each noise. In this pre-analysis, the data and the model include white noise, but the parameter of the white noise is fixed.

Figure B.1 shows the posterior probability distribution of the frequency and the amplitude of the FDM signal. Since it is redundant to plot the other parameters, the posterior distribution has been marginalized over them. The top and bottom plots are plots with and without the design matrix, respectively. The plot on the left uses the Data1, and the one on the right uses Data2. The two-dimensional contour plot represents the posterior probability distribution of the two parameters, and each solid and dashed line represent the 68% and the 95% credible region, respectively. The one-dimensional plot represents the the posterior probability distribution marginalized either one of the parameters, and the value above it is the MAP value. The brue vertical and horizontal lines denote the value of simulated data parameters.

For the case where TM noise is included in the model, It can be seen that the signal of the FDM can be detected when the frequency is $10^{-8.0}$ Hz. On the other hand, when the frequency is $10^{-8.55}$ Hz, the FDM can not be detected. The frequency has no peak in all region of the prior probability distribution, and the amplitude has a peak but the MAP value is not accurately determined. Since the amplitude has a finite value up to the lower limit of the prior probability distribution, the Bayes factor can be calculated. As a result, it is found that the value of Bayes factor is less than 1, so that the model which does not include the FDM is superior to the model which include it. By including the TM noise into the model we found that the low frequency signal of the FDM was not detected in the data we made, but we believe that there is no problem for the purpose of giving the upper limit. For the case where TM noise is not included in the model, it can be seen that the signal of the FDM is detected at either frequency. The uncertainty of the pre-analysis of the red noise and the SSE noise creates a bias, but the MAP values and the values of the simulated data parameters are very close. Therefore, we conclude that our implementation was done correctly.

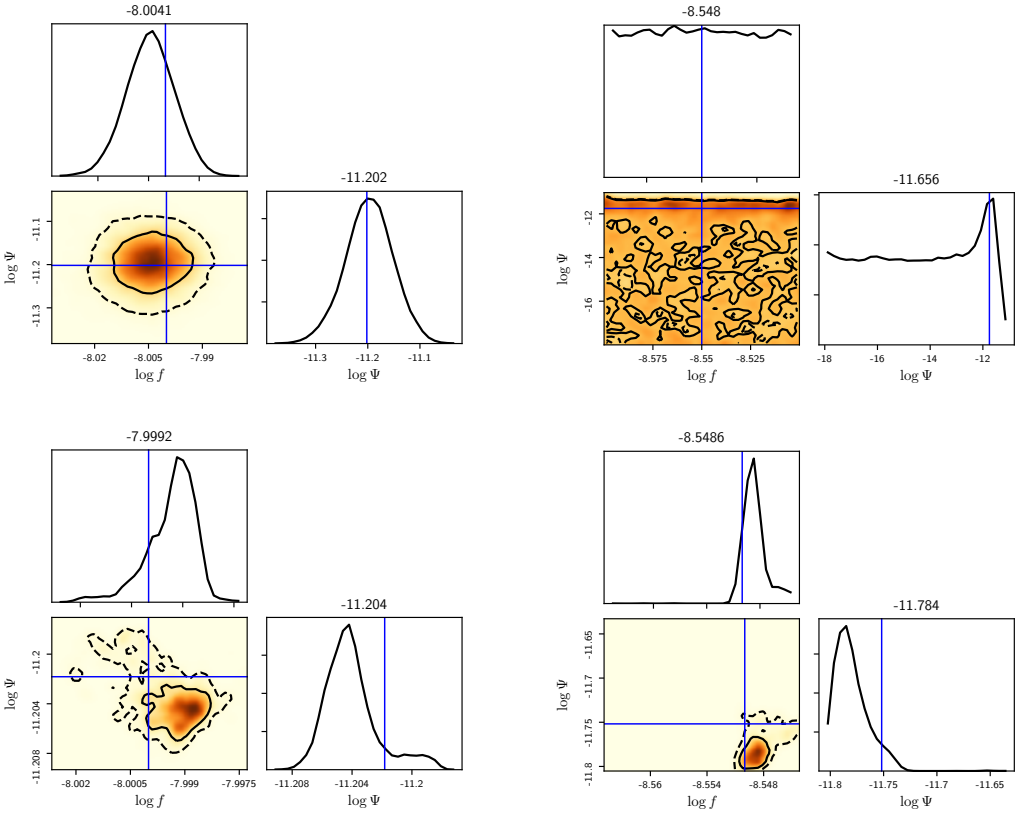

Figure B.1: The posterior probability distribution of the frequency and the amplitude of the FDM signal. The top and bottom plots are for the model with and without TM noise, respectively. The left and right plots are for the data with frequencies $10^{-8.0}$ and $10^{-8.55}$ Hz, respectively. The one-dimensional plot shows the posterior probability distribution marginalized over either the frequency or the amplitude, and the value above the plot denotes the MAP value. The two-dimensional contour plot shows the posterior probability distribution of the frequency or the amplitude, and each solid and dashed line represent the 68% and the 95% credible region, respectively. The blue vertical and horizontal lines denote the value of simulated data parameters.

Bibliography

[1] Peter Svrcek and Edward Witten. Axions In String Theory. *JHEP*, 06:051, 2006.

[2] Asimina Arvanitaki, Savas Dimopoulos, Sergei Dubovsky, Nemanja Kaloper, and John March-Russell. String Axiverse. *Phys. Rev.*, D81:123530, 2010.

[3] Wayne Hu, Rennan Barkana, and Andrei Gruzinov. Fuzzy cold dark matter: The wave properties of ultralight particles. *Phys. Rev. Lett.*, 85:1158–1161, Aug 2000.

[4] David J. E. Marsh. Axion Cosmology. *Phys. Rept.*, 643:1–79, 2016.

[5] Andrei Khmelnitsky and Valery Rubakov. Pulsar timing signal from ultralight scalar dark matter. *Journal of Cosmology and Astroparticle Physics*, 2014(02):019–019, feb 2014.

[6] Michael Kramer and David J Champion. The european pulsar timing array and the large european array for pulsars. *Classical and Quantum Gravity*, 30(22):224009, nov 2013.

[7] M A McLaughlin. The north american nanohertz observatory for gravitational waves. *Classical and Quantum Gravity*, 30(22):224008, nov 2013.

[8] R. N. Manchester, G. Hobbs, M. Bailes, W. A. Coles, W. van Straten, M. J. Keith, R. M. Shannon, N. D. R. Bhat, A. Brown, S. G. Burke-Spolaor, and et al. The parkes pulsar timing array project. *Publications of the Astronomical Society of Australia*, 30:e017, 2013.

[9] G Hobbs, A Archibald, Z Arzoumanian, D Backer, M Bailes, N D R Bhat, M Burgay, S Burke-Spolaor, D Champion, I Cognard, W Coles, J Cordes, P Demorest, G Desvignes, R D Ferdman, L Finn, P Freire, M Gonzalez, J Hessels, A Hotan, G Janssen, F Jenet, A Jessner, C Jordan, V Kaspi, M Kramer, V Kondratiev, J Lazio, K Lazaridis, K J Lee, Y Levin, A Lommen, D Lorimer, R Lynch, A Lyne, R Manchester, M McLaughlin, D Nice, S Oslowski, M Pilia, A Possenti, M Purver, S Ransom, J Reynolds, S Sanidas, J Sarkissian, A Sesana, R Shannon, X Siemens, I Stairs, B Stappers, D Stinebring, G Theureau, R van Haasteren, W van Straten, J P W Verbiest, D R B Yardley, and X P You. The international pulsar timing array project: using pulsars as a gravitational wave detector. *Classical and Quantum Gravity*, 27(8):084013, apr 2010.

[10] N. K. Porayko and K. A. Postnov. Constraints on ultralight scalar dark matter from pulsar timing. *Phys. Rev. D*, 90:062008, Sep 2014.

[11] Nataliya K. Porayko et al. Parkes Pulsar Timing Array constraints on ultralight scalar-field dark matter. *Phys. Rev.*, D98(10):102002, 2018.

[12] Takeshi Kobayashi, Riccardo Murgia, Andrea De Simone, Vid Iršič, and Matteo Viel. Lyman-α constraints on ultralight scalar dark matter: Implications for the early and late universe. *Physical Review D*, 96(12):123514, Dec 2017.

[13] Alberto Diez-Tejedor and David J. E. Marsh. Cosmological production of ultralight dark matter axions. 2017.

[14] Lam Hui, Jeremiah P. Ostriker, Scott Tremaine, and Edward Witten. Ultralight scalars as cosmological dark matter. *Phys. Rev. D*, 95:043541, Feb 2017.

[15] Laura G. Book and Eanna E. Flanagan. Astrometric Effects of a Stochastic Gravitational Wave Background. *Phys. Rev.*, D83:024024, 2011.

[16] Kimihiro Nomura, Asuka Ito, and Jiro Soda. Pulsar timing residual induced by ultralight vector dark matter. 2019.

[17] D. N. Matsakis, J. H. Taylor, and T. M. Eubanks. A statistic for describing pulsar and clock stabilities. *A&A*, 326:924–928, October 1997.

[18] E. Keane, B. Bhattacharyya, M. Kramer, B. Stappers, S. Bates, M. Burgay, Shami Chatterjee, D. Champion, R. Eatough, J. Hessels, G. Janssen, Kejia Lee, J. Leeuwen, J. Margueron, M. Oertel, Andrea Possenti, S. Ransom, Gilles Theureau, and Pablo Torne. A cosmic census of radio pulsars with the ska. 12 2014.

[19] Roger W. Romani. *Timing a Millisecond Pulsar Array*, pages 113–117. Springer Netherlands, 1989.

[20] R. S. Foster and D. C. Backer. Constructing a pulsar timing array. *The Astrophysical Journal*, 361:300–308, September 1990.

[21] J. P. W. Verbiest, L. Lentati, G. Hobbs, R. van Haasteren, P. B. Demorest, G. H. Janssen, J. B. Wang, G. Desvignes, R. N. Caballero, M. J. Keith, D. J. Champion, Z. Arzoumanian, S. Babak, C. G. Bassa, N. D. R. Bhat, A. Brazier, P. Brem, M. Burgay, S. Burke-Spolaor, S. J. Chamberlin, S. Chatterjee, B. Christy, I. Cognard, J. M. Cordes, S. Dai, T. Dolch, J. A. Ellis, R. D. Ferdman, E. Fonseca, J. R. Gair, N. E. Garver-Daniels, P. Gentile, M. E. Gonzalez, E. Graikou, L. Guillemot, J. W. T. Hessels, G. Jones, R. Karuppusamy, M. Kerr, M. Kramer, M. T. Lam, P. D. Lasky, A. Lassus, P. Lazarus, T. J. W. Lazio, K. J. Lee, L. Levin, K. Liu, R. S. Lynch, A. G. Lyne, J. Mckee, M. A. McLaughlin, S. T. McWilliams, D. R. Madison, R. N. Manchester, C. M. F. Mingarelli, D. J. Nice, S. Osłowski, N. T. Palliyaguru, T. T. Pennucci, B. B. P. Perera, D. Perrodin, A. Possenti, A. Petiteau,

S. M. Ransom, D. Reardon, P. A. Rosado, S. A. Sanidas, A. Sesana, G. Shaifullah, R. M. Shannon, X. Siemens, J. Simon, R. Smits, R. Spiewak, I. H. Stairs, B. W. Stappers, D. R. Stinebring, K. Stovall, J. K. Swiggum, S. R. Taylor, G. Theureau, C. Tiburzi, L. Toomey, M. Vallisneri, W. van Straten, A. Vecchio, Y. Wang, L. Wen, X. P. You, W. W. Zhu, and X. J. Zhu. The International Pulsar Timing Array: First data release. *Monthly Notices of the Royal Astronomical Society*, 458(2):1267–1288, May 2016.

[22] Peter Dewdney, Peter Hall, R Schillizzi, and J Lazio. The square kilometre array. *Proceedings of the Institute of Electrical and Electronics Engineers IEEE*, 97(8):1482–1496, 2009.

[23] Russell T. Edwards, G. B. Hobbs, and R. N. Manchester. Tempo2, a new pulsar timing package. 2. The timing model and precision estimates. *Mon. Not. Roy. Astron. Soc.*, 372:1549–1574, 2006.

[24] G. B. Hobbs, R. T. Edwards, and R. N. Manchester. tempo2, a new pulsar-timing package – i. an overview. *Monthly Notices of the Royal Astronomical Society*, 369(2):655–672, 2006.

[25] E. M. Standish. Time scales in the JPL and CfA ephemerides. *A&A*, 336:381–384, Aug 1998.

[26] A. W. Irwin and T. Fukushima. A numerical time ephemeris of the Earth. *A&A*, 348:642–652, Aug 1999.

[27] W. M. Folkner and R. S. Park. JPL planetary and Lunar ephemeris DE436. *Jet Propulsion Laboratory*, September 2016.

[28] L. Fairhead and P. Bretagnon. An analytical formula for the time transformation TB-TT. *A&A*, 229:240–247, Mar 1990.

[29] A. Lyne, F. Graham-Smith, and F. Graham-Smith. *Pulsar Astronomy*. Cambridge Astrophysics. Cambridge University Press, 2012.

[30] D. C. Backer and R. W. Hellings. Pulsar timing and general relativity. *ARA&A*, 24:537–575, Jan 1986.

[31] M. Maggiore. *Gravitational Waves: Volume 1: Theory and Experiments*. Gravitational Waves. OUP Oxford, 2008.

[32] The NANOGrav Collaboration, Z. Arzoumanian, A. Brazier, S. Burke-Spolaor, S. Chamberlin, S. Chatterjee, B. Christy, J. M. Cordes, N. Cornish, K. Crowter, P. B. Demorest, T. Dolch, J. A. Ellis, R. D. Ferdman, E. Fonseca, N. Garver-Daniels, M. E. Gonzalez, F. A. Jenet, G. Jones, M. L. Jones, V. M. Kaspi, M. Koop, M. T. Lam, T. J. W. Lazio, L. Levin, A. N. Lommen, D. R. Lorimer, J. Luo, R. S. Lynch, D. Madison, M. A. McLaughlin, S. T. McWilliams, D. J. Nice, N. Palliyaguru, T. T.

Pennucci, S. M. Ransom, X. Siemens, I. H. Stairs, D. R. Stinebring, K. Stovall, J. K. Swiggum, M. Vallisneri, R. van Haasteren, Y. Wang, and W. Zhu. The NANOGrav Nine-year Data Set: Observations, Arrival Time Measurements, and Analysis of 37 Millisecond Pulsars. *The Astrophysical Journal*, 813:65, November 2015.

[33] T. Damour and N. Deruelle. General relativistic celestial mechanics of binary systems. I. The post-Newtonian motion. *Ann. Inst. Henri Poincaré Phys. Théor*, 43(1):107–132, Jan 1985.

[34] Ch. Lange, F. Camilo, N. Wex, M. Kramer, D. C. Backer, A. G. Lyne, and O. Doroshenko. Precision timing measurements of PSR J1012+5307. *Monthly Notices of the Royal Astronomical Society*, 326(1):274–282, Sep 2001.

[35] Zaven Arzoumanian et al. The NANOGrav 11-year Data Set: High-precision timing of 45 Millisecond Pulsars. *Astrophys. J. Suppl.*, 235(2):37, 2018.

[36] R. Blandford, R. Narayan, and R. W. Romani. Arrival-time analysis for a millisecond pulsar. *Journal of Astrophysics and Astronomy*, 5:369–388, December 1984.

[37] Curt Cutler, Sarah Burke-Spolaor, Michele Vallisneri, Joseph Lazio, and Walid Majid. The Gravitational-Wave Discovery Space of Pulsar Timing Arrays. *Phys. Rev.*, D89(4):042003, 2014.

[38] Z. Arzoumanian et al. The NANOGrav 11-year Data Set: Pulsar-timing Constraints On The Stochastic Gravitational-wave Background. *Astrophys. J.*, 859(1):47, 2018.

[39] W. M. Folkner, J. G. Williams, D. H. Boggs, R. S. Park, and P. Kuchynka. The Planetary and Lunar Ephemerides DE430 and DE431. *Interplanetary Network Progress Report*, 196:1–81, February 2014.

[40] J. B. Wang et al. Comparison of Pulsar Positions from Timing and Very Long Baseline Astrometry. *Mon. Not. Roy. Astron. Soc.*, 469(1):425–434, 2017.

[41] Fabrizio Nesti and Paolo Salucci. The dark matter halo of the milky way, AD 2013. *Journal of Cosmology and Astroparticle Physics*, 2013(07):016–016, jul 2013.

[42] M. T. Lam, J. M. Cordes, S. Chatterjee, Z. Arzoumanian, K. Crowter, P. B. Demorest, T. Dolch, J. A. Ellis, R. D. Ferdman, E. Fonseca, M. E. Gonzalez, G. Jones, M. L. Jones, L. Levin, D. R. Madison, M. A. McLaughlin, D. J. Nice, T. T. Pennucci, S. M. Ransom, R. M. Shannon, X. Siemens, I. H. Stairs, K. Stovall, J. K. Swiggum, and W. W. Zhu. The NANOGrav Nine-year Data Set: Excess Noise in Millisecond Pulsar Arrival Times. *The Astrophysical Journal*, 834:35, January 2017.

[43] P. E. Boynton, E. J. Groth, D. P. Hutchinson, G. P. Nanos, Jr., R. B. Partridge, and D. T. Wilkinson. Optical Timing of the Crab Pulsar, NP 0532. *The Astrophysical Journal*, 175:217, July 1972.

[44] E. J. Groth. Timing of the Crab Pulsar III. The Slowing Down and the Nature of the Random Process. *The Astrophysical Journal Supplement Series*, 29, November 1975.

[45] Ryan M. Shannon and James M. Cordes. Assessing the role of spin noise in the precision timing of millisecond pulsars. *The Astrophysical Journal*, 725(2):1607, 2010.

[46] Andrew Lyne, George Hobbs, Michael Kramer, Ingrid Stairs, and Ben Stappers. Switched magnetospheric regulation of pulsar spin-down. *Science*, 329(5990):408–412, 2010.

[47] R. M. Shannon, J. M. Cordes, T. S. Metcalfe, T. J. W. Lazio, I. Cognard, G. Desvignes, G. H. Janssen, A. Jessner, M. Kramer, K. Lazaridis, M. B. Purver, B. W. Stappers, and G. Theureau. An Asteroid Belt Interpretation for the Timing Variations of the Millisecond Pulsar B1937+21. *The Astrophysical Journal*, 766:5, March 2013.

[48] M. T. Lam, J. M. Cordes, S. Chatterjee, Z. Arzoumanian, K. Crowter, P. B. Demorest, T. Dolch, J. A. Ellis, R. D. Ferdman, E. F. Fonseca, M. E. Gonzalez, G. Jones, M. L. Jones, L. Levin, D. R. Madison, M. A. McLaughlin, D. J. Nice, T. T. Pennucci, S. M. Ransom, X. Siemens, I. H. Stairs, K. Stovall, J. K. Swiggum, and W. W. Zhu. The NANOGrav Nine-year Data Set: Noise Budget for Pulsar Arrival Times on Intraday Timescales. *The Astrophysical Journal*, 819:155, March 2016.

[49] F. A. Jenet, G. B. Hobbs, W. van Straten, R. N. Manchester, M. Bailes, J. P. W. Verbiest, R. T. Edwards, A. W. Hotan, J. M. Sarkissian, and S. M. Ord. Upper bounds on the low-frequency stochastic gravitational wave background from pulsar timing observations: Current limits and future prospects. *The Astrophysical Journal*, 653(2):1571, 2006.

[50] G. Hobbs, F. Jenet, K. J. Lee, J. P. W. Verbiest, D. Yardley, R. Manchester, A. Lommen, W. Coles, R. Edwards, and C. Shettigara. TEMPO2, a new pulsar timing package. III: Gravitational wave simulation. *Mon. Not. Roy. Astron. Soc.*, 394:1945, 2009.

[51] Lindley Lentati, P. Alexander, M. P. Hobson, S. Taylor, J. Gair, S. T. Balan, and R. van Haasteren. Hyper-efficient model-independent Bayesian method for the analysis of pulsar timing data. *Phys. Rev.*, D87(10):104021, 2013.

[52] Z. Arzoumanian, A. Brazier, S. Burke-Spolaor, S. J. Chamberlin, S. Chatterjee, J. M. Cordes, P. B. Demorest, X. Deng, T. Dolch, J. A. Ellis, R. D. Ferdman, N. Garver-Daniels, F. Jenet, G. Jones, V. M. Kaspi, M. Koop, M. T. Lam, T. J. W. Lazio, A. N. Lommen, D. R. Lorimer, J. Luo, R. S. Lynch, D. R. Madison, M. A. McLaughlin, S. T. McWilliams, D. J. Nice, N. Palliyaguru, T. T. Pennucci, S. M. Ransom, A. Sesana, X. Siemens, I. H. Stairs, D. R. Stinebring, K. Stovall, J. Swiggum, M. Vallisneri, R. van Haasteren, Y. Wang, , W. W. Zhu, and NANOGrav

Collaboration. Gravitational waves from individual supermassive black hole binaries in circular orbits: Limits from the north american nanohertz observatory for gravitational waves. *The Astrophysical Journal*, 794(2):141, 2014.

[53] Ellis J. *Searching for Gravitational Waves Using Pulsar Timing Arrays*. PhD thesis, The Univ. Wisconsin-Milwaukee, 2014.

[54] S. R. Taylor, L. Lentati, S. Babak, P. Brem, J. R. Gair, A. Sesana, and A. Vecchio. All correlations must die: Assessing the significance of a stochastic gravitational-wave background in pulsar-timing arrays. *Phys. Rev.*, D95(4):042002, 2017.

[55] R. W. Hellings and G. S. Downs. Upper limits on the isotropic gravitational radiation background from pulsar timing analysis. *The Astrophysical Journal, Letters*, 265:L39–L42, February 1983.

[56] D. J. Champion, G. B. Hobbs, R. N. Manchester, R. T. Edwards, D. C. Backer, M. Bailes, N. D. R. Bhat, S. Burke-Spolaor, W. Coles, P. B. Demorest, R. D. Ferdman, W. M. Folkner, A. W. Hotan, M. Kramer, A. N. Lommen, D. J. Nice, M. B. Purver, J. M. Sarkissian, I. H. Stairs, W. van Straten, J. P. W. Verbiest, and D. R. B. Yardley. Measuring the mass of solar system planets using pulsar timing. *The Astrophysical Journal Letters*, 720(2):L201, 2010.

[57] D. Brouwer and G.M. Clemence. *Methods of celestial mechanics*. Academic Press, 1961.

[58] T. Joseph W. Lazio, S. Bhaskaran, C. Cutler, W. M. Folkner, R. S. Park, J. A. Ellis, T. Ely, S. R. Taylor, and M. Vallisneri. Solar System Ephemerides, Pulsar Timing, Gravitational Waves, & Navigation. *IAU Symp.*, 337:150–153, 2017.

[59] Brian Luzum, Nicole Capitaine, Agnès Fienga, William Folkner, Toshio Fukushima, James Hilton, Catherine Hohenkerk, George Krasinsky, Gérard Petit, Elena Pitjeva, Michael Soffel, and Patrick Wallace. The iau 2009 system of astronomical constants: the report of the iau working group on numerical standards for fundamental astronomy. *Celestial Mechanics and Dynamical Astronomy*, 110(4):293, Jul 2011.

[60] Phil Gregory. *Bayesian Logical Data Analysis for the Physical Sciences: A Comparative Approach with Mathematica® Support*. Cambridge University Press, 2005.

[61] A. Gelman, J.B. Carlin, H.S. Stern, D.B. Dunson, A. Vehtari, and D.B. Rubin. *Bayesian Data Analysis, Third Edition*. Chapman & Hall/CRC Texts in Statistical Science. Taylor & Francis, 2013.

[62] R. A. Jacobson. The orbits of the uranian satellites and rings, the gravity field of the uranian system, and the orientation of the pole of uranus. *The Astronomical Journal*, 148(5):76, 2014.

[63] Z. Arzoumanian, A. Brazier, S. Burke-Spolaor, S. J. Chamberlin, S. Chatterjee, B. Christy, J. M. Cordes, N. J. Cornish, K. Crowter, P. B. Demorest, X. Deng, T. Dolch, J. A. Ellis, R. D. Ferdman, E. Fonseca, N. Garver-Daniels, M. E. Gonzalez, F. Jenet, G. Jones, M. L. Jones, V. M. Kaspi, M. Koop, M. T. Lam, T. J. W. Lazio, L. Levin, A. N. Lommen, D. R. Lorimer, J. Luo, R. S. Lynch, D. R. Madison, M. A. McLaughlin, S. T. McWilliams, C. M. F. Mingarelli, D. J. Nice, N. Palliyaguru, T. T. Pennucci, S. M. Ransom, L. Sampson, S. A. Sanidas, A. Sesana, X. Siemens, J. Simon, I. H. Stairs, D. R. Stinebring, K. Stovall, J. Swiggum, S. R. Taylor, M. Vallisneri, R. van Haasteren, Y. Wang, W. W. Zhu, and The NANOGrav Collaboration. The nanograv nine-year data set: Limits on the isotropic stochastic gravitational wave background. *The Astrophysical Journal*, 821(1):13, 2016.

[64] Justin Ellis and Rutger van Haasteren. jellis18/ptmcmcsampler: Official release, October 2017.

[65] Justin Ellis and Rutger van Haasteren. jellis18/pal2: Pal2, January 2017.

[66] Heikki Haario, Eero Saksman, and Johanna Tamminen. An adaptive metropolis algorithm. *Bernoulli*, 7(2):223–242, 2001.

[67] Heikki Haario, Eero Saksman, and Johanna Tamminen. Componentwise adaptation for high dimensional mcmc. *Computational Statistics*, 20(2):265–273, 2005.

[68] Cajo JF Ter Braak. A markov chain monte carlo version of the genetic algorithm differential evolution: easy bayesian computing for real parameter spaces. *Statistics and Computing*, 16(3):239–249, 2006.

[69] S. Vaughan, P. Uttley, A. G. Markowitz, D. Huppenkothen, M. J. Middleton, W. N. Alston, J. D. Scargle, and W. M. Farr. False periodicities in quasar time-domain surveys. *Mon. Not. Roy. Astron. Soc.*, 461(3):3145–3152, 2016.

[70] J. Kruschke. *Doing Bayesian Data Analysis: A Tutorial Introduction with R*. Elsevier Science, 2010.

[71] H. Jeffreys. *The Theory of Probability*. Clarenson Press, 2nd edition, 1948.

[72] Robert E. Kass and Adrian E. Raftery. Bayes factors. *Journal of the American Statistical Association*, 90(430):773–795, 1995.

[73] Adrian E. Raftery. Bayesian model selection in social research. *Sociological Methodology*, 25:111–163, 1995.

[74] A. O'Hagan and M. Kendall. *Kendall's advanced theory of statistics: Vol. IIB*. Edward Arnold, 1994.

[75] James M. Dickey. The weighted likelihood ratio, linear hypotheses on normal location parameters. *The Annals of Mathematical Statistics*, 42(1):204–223, 1971.

[76] Isabella Verdinelli and Larry Wasserman. Computing bayes factors using a generalization of the savage-dickey density ratio. *Journal of the American Statistical Association*, 90(430):614–618, 1995.